Global Biogeochemical Cycles

RESEARCH ARTICLE
10.1029/2023GB008009

Synthesis of In Situ Marine Calcium Carbonate Dissolution Kinetic Measurements in the Water Column

Ben A. Cala[1,2], **Olivier Sulpis**[3], **Mariette Wolthers**[2], **and Matthew P. Humphreys**[1]

[1]Department of Ocean Systems (OCS), NIOZ Royal Netherlands Institute for Sea Research, Texel, The Netherlands, [2]Department of Earth Sciences, Utrecht University, Utrecht, The Netherlands, [3]CEREGE, Aix Marseille University, CNRS, IRD, INRAE, Aix-en-Provence, France

Key Points:

- Published in situ carbonate mineral dissolution rate measurements in the water column are compiled and the saturation state (Ω) is estimated
- Dissolution rates differ by 2 orders of magnitude at the same Ω, mainly due to differences in experimental design between the studies
- The compiled data set is used to investigate dissolution above the saturation horizon and to validate laboratory observations

Supporting Information:

Supporting Information may be found in the online version of this article.

Correspondence to:

B. A. Cala,
ben.cala@nioz.nl

Citation:

Cala, B. A., Sulpis, O., Wolthers, M., & Humphreys, M. P. (2024). Synthesis of in situ marine calcium carbonate dissolution kinetic measurements in the water column. *Global Biogeochemical Cycles*, *38*, e2023GB008009. https://doi.org/10.1029/2023GB008009

Received 20 OCT 2023
Accepted 14 JUL 2024

Author Contributions:

Conceptualization: Ben A. Cala, Olivier Sulpis, Mariette Wolthers, Matthew P. Humphreys
Data curation: Ben A. Cala
Formal analysis: Ben A. Cala
Funding acquisition: Olivier Sulpis, Mariette Wolthers, Matthew P. Humphreys
Investigation: Ben A. Cala
Methodology: Ben A. Cala, Matthew P. Humphreys
Project administration: Olivier Sulpis, Mariette Wolthers, Matthew P. Humphreys
Software: Ben A. Cala

Abstract Calcium carbonate ($CaCO_3$) dissolution is an integral part of the ocean's carbon cycle. However, laboratory measurements and ocean alkalinity budgets disagree on the rate and loci of dissolution. In situ dissolution studies can help to bridge this gap, but so far published studies have not been utilized as a whole because they have not previously been compiled into one data set and lack carbonate system data to compare between studies. Here, we compile all published measurements of $CaCO_3$ dissolution rates in the water column (11 studies, 752 data points). Combining World Ocean Atlas data (temperature, salinity) with the neural network CANYON-B (carbonate system variables), we estimate seawater saturation state (Ω) for each rate measurement. We find that dissolution rates at the same Ω vary by 2 orders of magnitude. Using a machine learning approach, we show that while Ω is the main driver of dissolution rate, most variability can be attributed to differences in experimental design, above all bias due to (diffusive) transport and the synthetic or biogenic nature of $CaCO_3$. The compiled data set supports previous findings of a change in the mechanism driving dissolution at $\Omega_{crit} = 0.8$ that separates two distinct dissolution regimes: $r_{slow} = 0.29 \cdot (1 - \Omega)^{0.68(\pm 0.16)}$ mass% day^{-1} and $r_{fast} = 2.95 \cdot (1 - \Omega)^{2.2(\pm 0.2)}$ mass% day^{-1}. Above the saturation horizon, one study shows significant dissolution that cannot solely be explained by established theories such as zooplankton grazing and organic matter degradation. This suggests that other, non-biological factors may play a role in shallow dissolution.

1. Introduction

Marine carbonate minerals such as calcium carbonate ($CaCO_3$) play an integral role in the Earth's carbon cycle, regulating the oceanic uptake of CO_2 and acting as a buffer against anthropogenic ocean acidification (Archer et al., 2009; Zeebe & Wolf-Gladrow, 2001). The increase of atmospheric CO_2 lowers the ocean's pH, which enhances the dissolution of carbonate minerals, increasing the ocean's alkalinity. The depth of $CaCO_3$ dissolution influences the timescale on which the ocean can mitigate the drastic increase in anthropogenic CO_2: regeneration of alkalinity in the shallow ocean affects atmospheric CO_2 more immediately than in the deep sea, from where the regenerated alkalinity first needs to be transported into surface waters.

Despite its importance, marine $CaCO_3$ production and dissolution are still poorly constrained (Liang et al., 2023). Marine $CaCO_3$ most commonly occurs in the forms of calcite (e.g., foraminifera and coccolithophores) and aragonite (e.g., pteropods). While most studies focus on calcite, there is growing evidence that the more soluble aragonite makes a major contribution to $CaCO_3$ cycling, with aragonite estimated to contribute up to 20% to particulate inorganic carbon (PIC) flux (Knecht et al., 2023; Neukermans et al., 2023). The magnesium-rich form of calcite (high-Mg calcite), produced by some foraminifera, algae and teleosts, has also been proposed to play an important role (Wilson et al., 2009; Woosley et al., 2012), but its contribution remains unquantified.

Additionally, seawater alkalinity measurements provide evidence that the majority of pelagic $CaCO_3$ dissolution occurs in waters that are supersaturated with respect to both calcite and aragonite and therefore in theory dissolution should not occur (Feely et al., 2002; Sulpis et al., 2021). Specifically, biogeochemical budgets reveal an excess of alkalinity in these waters that can only be explained by carbonate mineral dissolution (e.g., Milliman et al., 1999). Although several mechanisms have been proposed, including dissolution in low-pH, metabolic microenvironments (e.g., Jansen & Wolf-Gladrow, 2001; Subhas et al., 2022) and dissolution of more soluble phases such as aragonite or high-Mg calcite (e.g., Knecht et al., 2023; Wilson et al., 2009), a complete explanation for apparent dissolution above the saturation horizon remains elusive.

The dissolution rate depends on the water's saturation state (Ω) for each mineral:

Supervision: Olivier Sulpis, Mariette Wolthers, Matthew P. Humphreys
Validation: Ben A. Cala
Visualization: Ben A. Cala
Writing – original draft: Ben A. Cala, Olivier Sulpis, Mariette Wolthers, Matthew P. Humphreys
Writing – review & editing: Olivier Sulpis, Mariette Wolthers, Matthew P. Humphreys

$$\Omega = \frac{\left[\mathrm{Ca}^{2+}\right]\left[\mathrm{CO_3}^{2-}\right]}{K^*_{\mathrm{sp}}} \tag{1}$$

where square brackets indicate the concentration of the enclosed species and with the solubility product

$$K^*_{\mathrm{sp}} = \left[\mathrm{Ca}^{2+}\right]\left[\mathrm{CO_3}^{2-}\right]_{\mathrm{sat}} \tag{2}$$

a function of temperature (T), salinity (S), and pressure which is different for each mineral. The kinetics of carbonate mineral dissolution with respect to Ω have mainly been assessed in laboratory settings (Gehlen et al., 2005; Keir, 1980; Morse & Berner, 1972; Naviaux, Subhas, Rollins, et al., 2019; Subhas et al., 2015), although more recently in situ measurements have also been used (Dong et al., 2019; Naviaux, Subhas, Dong, et al., 2019; Subhas et al., 2022). Measured dissolution rates (r) are canonically fitted to the function

$$r = k(1 - \Omega)^n \tag{3}$$

where k is the rate constant and n is the pseudo reaction order (Morse & Arvidson, 2002). Since K^*_{sp} increases with higher pressure and lower temperature (Hawley & Pytkowicz, 1969; Mucci, 1983), Ω decreases with depth and the highest dissolution rate is therefore expected in the deep ocean.

Peterson (1966) and Berger (1967) found that dissolution of calcite particles attached to a mooring in the Pacific started high in the water column but increased only slightly with depth until approximately 4,000 m, where dissolution suddenly began to increase rapidly. This was first explained through hydrodynamic influences such as current velocity (Edmond, 1974), but because this effect could also be observed in the laboratory (Keir, 1980; Morse & Berner, 1972), a change in reaction kinetics at the surface of the carbonate minerals at critical undersaturation soon became more a more accepted explanation (Milliman, 1977). While Teng (2004) in freshwater and Dong et al. (2020) in seawater, observed three distinct dissolution mechanisms, from step edge retreat, through defect-assisted etch pit formation to homogeneous etch pit formation with increasing undersaturation, Naviaux, Subhas, Rollins, et al. (2019) found that at the relevant temperatures in seawater (5°C), the mechanism directly switches from step edge retreat to homogeneous etch pit formation at a critical saturation state $\Omega_{\mathrm{crit}} \approx 0.75$. For $\Omega_{\mathrm{crit}} < \Omega < 1$, dissolution is slower and less sensitive to the saturation state and for $\Omega < \Omega_{\mathrm{crit}}$ dissolution increases more rapidly with undersaturation. When $\Omega > 1$, seawater is oversaturated, so no dissolution should occur.

One issue with applying laboratory results to the real ocean is environmental complexity. While laboratory experiments happen in known and controlled environments, the ocean is complex with many (often biological) processes happening simultaneously under wide ranges of variable hydrographic conditions that cannot be comprehensively simulated in the laboratory. In situ studies of dissolution rates are controlled experiments where synthetic or sedimentary carbonate minerals are placed at certain depths in the water column and are therefore not representative of the fate of calcium carbonate produced in the surface ocean. They do, however, help to bridge the gap between laboratory experiments and oceanographic alkalinity data by implicitly including the effects of these processes and background variability, also helping to validate and inform future laboratory studies. Fewer than a dozen studies with in situ dissolution rate measurements have been conducted (Table 1). Due to the variety in the experimental design (Figure 1) and the rates being reported in mutually incompatible units, it is challenging to compare the results of in situ studies with each other and thus draw overall conclusions about real-world dissolution. Furthermore, much of the data in older publications is only presented in the form of depth-rate plots, with other variables describing the water chemistry (DIC, TA, pH, and Ω) and environment (salinity, temperature, and dissolved oxygen) around the sample either not recorded or not included. Therefore, the results of these in situ studies have mostly been considered individually and not systematically examined as a whole.

Here, we present a new compilation of (to the best of our knowledge) all published in situ marine carbonate dissolution measurements in the water column. For each measurement, we have estimated the set of hydrographic variables required to investigate dissolution temperature, salinity (S), dissolved oxygen, pH_T, total alkalinity (TA), dissolved inorganic carbon (DIC), and the saturation state of calcite (Ω_{ca}) and aragonite (Ω_{ar}) using the World Ocean Atlas 2018 (WOA18) data set together with the neural network CANYON-B (Bittig et al., 2018).

Table 1
Overview of the Methods of All Published Studies Measuring $CaCO_3$ Dissolution Rates In Situ in the Water Colμmn

Source	Abbrev.	Location	Duration	Cycling device?	Rate determination	Mesh size (μm)	Sample	Biogenic?	Cleaned?	Sample size
Peterson (1966)	P66	19N, 169W	4 months	No	Weight loss	–	Calcite crystal	No	–	cm-sized
Berger (1967)	B67	19N, 169W	4 months	No	Weight loss	62	Foraminfera assemblage	Yes	Yes	Unknown
							Foraminfera assemblage	Yes	No	Unknown
Milliman (1977)	M77	23N, 70W	4 months,	No	Weight loss	20–40	Foraminifera (O universa, G sacculifer)	Yes	No	250–500 μm (L)
		23N, 65W								
		23N, 55W	9 months				Aragonite ooids	No	–	
		26N, 60W					Mg Calicte ooids (12% Mg)	No	–	
Honjo and Erez (1978)	HE78	32N, 155W	79 days	Yes (0.6 mL/min)	Weight loss	0.4–0.6	Reagent calcite	No	–	10–53 μm (XXS)
							Large calcite crystal	No	–	0.7–1 mm (XXL)
							Synthetic aragonite	No	–	10–53 μm (XXS)
							Foraminfera assemblage	Yes	No	63–1,000 μm
							Foraminfera assemblage	Yes	Yes	63–1,000 μm
							G sacculifer	Yes	No	>250 μm (L)
							G bulloides	Yes	No	>250 μm (L)
							G pachyderma	Yes	No	>149 μm (M)
							E huxleyi	Yes	No	XXXS
							E huxleyi		Yes	XXXS
							C neohelis	Yes	No	XXXS
							Pteropod assemblage	Yes		>831 μm (XXL)
Thunell et al. (1981)	T81	4N, 82W	123 days	No	Weight loss, Fragmentation	100	Foraminfera assemblage	Yes	No	>250 μm (L)
Metzler et al. (1982)	M82	0N, 152W	123 days	No	Weight loss, Fragmentation	44	Foraminfera assemblage	Yes	Yes	62–125 μm (XS)
										125–177 μm (S)
										177–250 μm (M)
										250–420 μm (L)
										>420 μm (XL)
Troy et al. (1997)	T97	23N, 158W	3 days	No	Surface roughness	333	Calcite crystal	No	–	cm-sized
Fukuhara et al. (2008)	F08	30N, 175E	23 days	Most not, only at 2 depths (5 mL/min)	Weight loss	Most 63, some 30	Aragonite crystal	No	–	3 size fractions:
							Calcite crystal	No	–	125–250 μm (S),
							G sacculifer	Yes	No	250–425 μm (L),
							G inflata	Yes	No	425–500 μm (XL)
							G truncatulinoides	Yes	No	
CDisK-IV	D19	28N, 155W	24–58 hr	Yes (5 mL/min)	d13C	8	Synthetic Aragonite	No	–	250–495 μm (L)
		35N, 151W								
	N19	42N, 148W				8	Synthetic Calcite	No	–	20–53 μm (XXS)
	S22	50N, 155W				0.8	E huxleyi	Yes	Yes	XXXS

Note. "*Cleaned?*" refers to whether the sample underwent an oxidative cleaning protocol to remove organic coatings.

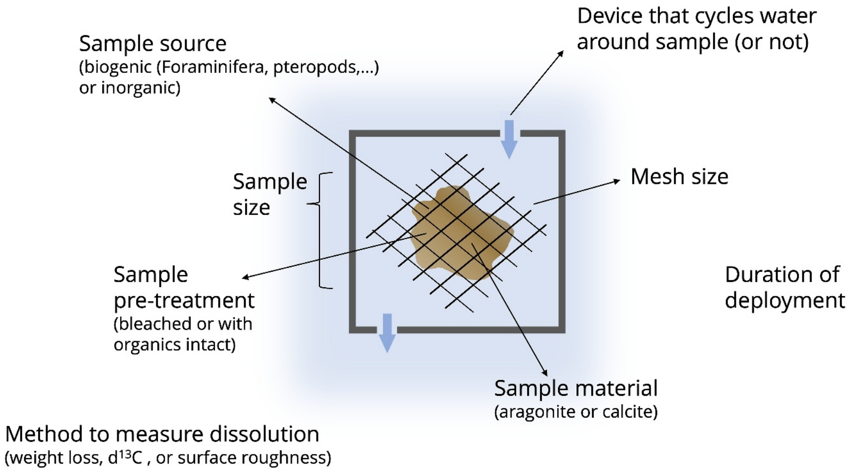

Figure 1. Overview of how experimental design can vary between the different studies for in situ dissolution measurements. Half of the categories describe the setup of the experiment: the duration of the samples' deployment in the water column, whether a device was employed to cycle water around the sample to avoid stagnation effects, and what method was used to determine how much dissolution took place. Mesh size refers to the size of the openings in the fine mesh the sample was placed into during deployment. The other categories describe the sample itself. The sample source refers to whether the sample was inorganic (e.g., calcite crystal) or biogenic (e.g., the shell of a pteropod). Sample pre-treatment refers to the oxidative cleaning which some experiments conducted on the biogenic samples to remove any organic coatings that might have still been intact. The material is either aragonite (e.g., pteropods) or calcite (e.g., foraminifera). The size of the sample refers to the diameter of one unit/grain of the sample.

We used a machine learning (ML) regression model to understand how much of the variability in the measured dissolution rate can be explained by each aspect of the experimental design (Figure 1) and in what way each aspect affects the dissolution rate. We use the compiled data set to assess whether significant dissolution above the saturation horizon has been observed by in situ studies. Additionally, we validate laboratory measurements of different dissolution regimes based on the degree of undersaturation.

2. Methods

2.1. Data Compilation

First, the dissolution rates from the various in situ studies (Table 1) were compiled. To find suitable studies, we used various combinations of the keywords "dissolution rate" "calcite," "aragonite, "foraminifera," "marine," "ocean," "in situ," "mooring," and "measurement" (e.g., "dissolution rate calcite in situ") in Google Scholar and Semantic Scholar. Since we focused on dissolution in the water column, we did not consider studies that determine dissolution rates from sediment cores (e.g., porewater measurements) or at the sediment-water interface. We also excluded studies that estimate dissolution rates from sediment trap samples. Beside the initial keyword-based searches, we identified additional studies by reviewing the references cited within the already selected papers. In studies where the dissolution rates were only reported in a figure instead of being tabulated, the data were extracted using WebPlotDigitizer (Rohatgi, 2021).

Where available, additional information such as percentage fragmentation of the sample (T81, M82), measurement uncertainty (P66, D19, N19, S22) and environmental variables (D19, N19, S22) were also retrieved, along with complementary information about the sample (material, biogenic, organic coating), experimental setup (water cycling device, particle size, mesh size), and measurement technique (for an overview in the differences of experimental design see Figure 1). As described in the accompanying paper (Metzler et al., 1982), the measurements from Station 2 in M82 were of low quality due to mechanical loss of the sample and are therefore not included in this compilation.

2.2. Estimation of Ω

In most cases, the dissolution rate was reported as a function of depth but with carbonate system variables for the surrounding seawater either not measured or not recorded, making it impossible to directly calculate the seawater saturation state. Instead, we developed a method to estimate Ω using the World Ocean Atlas 2018 (WOA18) and the neural network CANYON-B (Bittig et al., 2018) (Figure 2). The validation of this method is described in Supporting Information S1.

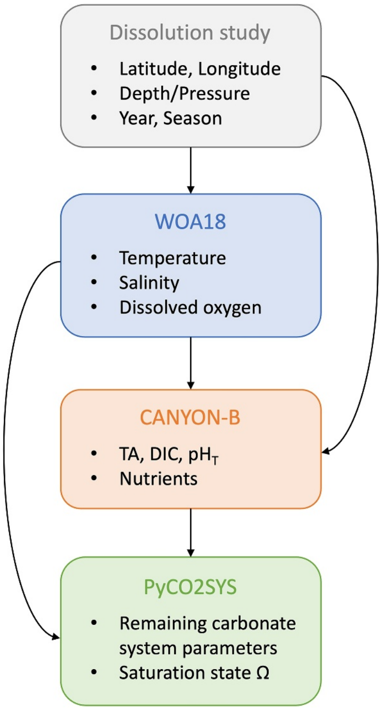

Figure 2. Summary of the workflow to estimate Ω. Starting from the top (Dissolution study), each box represents a workflow step in which the outputs listed inside the box were obtained. The arrows show where outputs from a step were used as inputs to a later step.

Temperature (Locarnini et al., 2018), salinity (Zweng et al., 2019), and dissolved oxygen data (Garcia et al., 2019) were taken from WOA18. For the upper 57 levels (1,500 m) we took the seasonal statistics and below that the annual averages of the objectively analyzed climatology (standard depth levels (102 levels, 0–5,500 m) at 1° resolution, using data from all available years ("all" or "decav" data sets)). The data at the grid point closest to the measurement site were interpolated over depth and appended to the compiled data.

This environmental data, as well as the geographic location and time of the expedition (for experiments lasting several months, we used the mid-point of the experiment), were used as input parameters for CANYON-B (Bittig et al., 2018). CANYON-B is a Bayesian neural network trained on the GLODAPv2 data set (Olsen et al., 2016) that calculates marine carbonate system variables (TA, DIC, pH) and nutrients (phosphate, silicate, nitrate) as a function of geographic location, time (month and year), depth, pressure, temperature, salinity, and dissolved oxygen. With these input parameters, CANYON-B captures both the measured relationship between the carbonate system and physical properties of seawater as well as the temporal changes throughout the water column due to anthropogenic increase of atmospheric CO_2, which results in higher DIC and lower pH values over the last decades.

Using the DIC-pH$_T$ pair as inputs, the remainder of the carbonate system, including Ω, was calculated with PyCO2SYS (version 1.8.1) (Humphreys et al., 2022) with the carbonic acid dissociation constants K_1 and K_2 of Sulpis et al. (2020), the borate:chlorinity of Uppström (1974), the K_{HSO4} of Dickson (1990), and the calcite and aragonite K_{sp} of Mucci (1983) together with the PyCO2SYS defaults for the other optional constants.

The only studies that reported hydrographic variables with their dissolution experiments were during the CDisK-IV cruise, which includes N19, D19, and S22. A comparison between CDisK-IV measurements (Berelson et al., 2022) and the values generated by our method described above can be found in Supporting Information S1 (Figures S9 and S10). For the analysis done in this study, the measured values from the CDisK-IV cruise experiments are used and in our final data compilation, both the measured and estimated values are reported.

2.3. Uncertainty Propagation

The uncertainty of Ω was estimated by propagating the uncertainties for each of the variables needed for its determination through each of the workflow steps (Figure 2).

The uncertainty associated with the variables obtained from WOA18 is represented by their standard deviation. We used the objectively analyzed climatology, which does not include a standard deviation. Therefore, we rely on the standard deviation of the statistical mean of the measurements that were made at that grid point at a certain standard depth level. We only considered standard deviations that were determined with enough measurements (>4) to yield a meaningful value.

For temperature and salinity, the standard deviation was calculated from a combination of seasonal data for the upper 1,500 m of the water column and annual data for the remaining depths. However, where the seasonal data set contained fewer than 5 measurements at any given depth, we used the annual mean for the entire water column. For dissolved oxygen, the number of measurements available was much lower, resulting in no valid standard deviations for most grid cells. In this case, we calculated the average of all standard deviations at grid points that had at least 5 measurements shallower than 1,500 m within a 10-degree radius around the experiment site. For all variables, if fewer than 5 measurements existed at deeper depth levels, the closest shallower valid standard deviation was used. Subsequently, the standard deviations were interpolated across depth and appended to the compiled data set.

The 90th percentile for the estimated uncertainty of TA, DIC, pH and nutrients inherent to CANYON-B, $\sigma^2_{\text{CANYON-B}}(m)$ is given by Bittig et al. (2018). We combined this with the uncertainty stemming from WOA18 from temperature (T), salinity (S), and dissolved oxygen ($[\mathrm{O_2}]$):

$$\sigma(m) = \sqrt{\left(\frac{\partial m(T)}{\partial T}\right)^2 \sigma^2(T) + \left(\frac{\partial m(S)}{\partial S}\right)^2 \sigma^2(S) + \left(\frac{\partial m([\mathrm{O_2}])}{\partial [\mathrm{O_2}]}\right)^2 \sigma^2([\mathrm{O_2}]) + \sigma^2_{\text{CANYON-B}}(m)} \tag{4}$$

The derivatives $\frac{\partial m(x)}{\partial x}$ were calculated by finite forward difference, with

$$\frac{\partial m(x)}{\partial x} = \frac{m(x + \Delta x) - m(x)}{\Delta x} \tag{5}$$

for which CANYON-B was run again with $x + \Delta x$. We chose $\Delta T = 0.001$°C, $\Delta S = 0.001$, and $\Delta[\mathrm{O_2}] = 0.001$ μmol $\mathrm{kg^{-1}}$ but the results were stable with Δx an order of magnitude larger or smaller.

We propagated the uncertainties in TA, DIC, temperature, salinity and nutrients through to Ω using the in-built uncertainty propagation tool in PyCO2SYS. In this step, we also included uncertainty stemming from the equilibrium constants of the carbonate system and the solubility products of calcite and aragonite, as implemented in PyCO2SYS following Orr et al. (2018). However, by default PyCO2SYS propagates uncertainties assuming that the uncertainty in each argument is independent, which is not the case here: for instance, temperature is used to calculate DIC and pH in CANYON-B, so their uncertainties will covary. However, this covariance has a negligible contribution to the overall uncertainty in CANYON-B outputs because the majority of their uncertainty arises from the inherent uncertainty in the CANYON-B model, rather than propagated uncertainties in its input variables, and is thus independent of the input uncertainties.

2.4. Feature Importance

To evaluate the contribution of different features of the experimental design to the measured dissolution rate, we used a supervised machine learning model to predict the dissolution rates of mass-normalized measurements.

The independent variables (predictors) were Ω and seven features describing the experimental design (Table 1 and Figure 1): (a) size fraction of the $\mathrm{CaCO_3}$ samples (in eight categories, from XXXS to XXL; Table S1 in Supporting Information S1), (b) mesh size, (c) whether the particle was inorganic or biogenic and whether it underwent an oxidative cleaning protocol to remove organic coatings, (d) if a water cycling device was used to avoid diffusion effects, (e) the deployment time of the $\mathrm{CaCO_3}$ sample, (f) mineral form (calcite or aragonite), and (g) the measurement method (weight loss or δ^{13}C). Dissolution measurements with missing data for any one of these predictors were excluded from the model.

A predictive regression model was implemented with the XGBoost (Extreme Gradient Boosting) library (version 1.7.1) (Chen & Guestrin, 2016). The XGBoost regressor is an ensemble machine learning model which is made up of multiple decision trees. A decision tree is a hierarchical model where data is continuously split based on a feature at a decision node, until finally reaching one of the leaf nodes that represent the possible outcomes of the model (Breiman et al., 1984). XGBoost utilizes a gradient boosting framework, where new trees are gradually added to the ensemble in such a way that the loss gradient (difference between predicted and actual outcome) is minimized. This approach is especially suited for capturing non-linear relationships and interactions between features.

The data set was randomly split into training and testing sets with a ratio of 80:20. To maximize model performance and avoid overfitting, the model parameters need to be tuned, for which the training set was further randomly split into five folds for cross-validation. A grid search was performed using the GridSearchCV function from the scikit-learn library (version 1.2.2) (Pedregosa et al., 2011) with R-squared ($\mathrm{R^2}$) as the scoring metric. Afterward, the XGBoost Regressor was trained on the entire training set with squared error as the learning objective using the optimal parameters (see Supporting Information S1) obtained in the previous step. The trained model was then evaluated on the testing set using R^2, the mean absolute error (MAE) and mean squared error (MSE) or root mean squared error (RMSE). For all steps (hyperparameter tuning, model training and evaluation) the data were weighted such that the total weight of each study was equal so that studies with a greater number of measurements did not have a greater influence on the model. Without this weighting, the differences between the data points of one study with many data points would overshadow the variations between different studies. Categorical data were encoded by mapping each unique label to an integer value.

Machine learning models are often regarded as "black boxes." Since their decision-making process is complicated with various layers, it is difficult to understand how the model arrives at certain predictions (Breiman, 2001b; Molnar, 2022). Two methods were employed here to gain insight into the importance and relationship of a specific feature to the model's prediction of dissolution rates: Permutation Feature Importance (PFI) (Breiman, 2001a) and Partial Dependence Plots (PDPs) (Friedman, 2001). For both, we used the implementation in the scikit-learn library (version 1.2.2). PFI randomly permutates the values of each feature and measures how much this decreases the model's performance. It gives insight into how relevant a feature is for the model to arrive at a correct prediction. PFI was calculated for the test data using mean squared error (MSE) as the scoring metric. PDPs show how changing a certain feature affects the model output by showing the relationship between each feature and the model's predictions while holding all other features constant. Thus, PDPs can also be used to identify non-linear relationships between features and the model's prediction.

2.5. Investigating Dissolution Regimes

When determining the reaction kinetics for dissolution, Equation 3 is linearized to

$$\log_{10} r = \log_{10} k + n \cdot \log_{10}(1 - \Omega) \tag{6}$$

With two dissolution regimes, the data must to be fitted to two linear functions of the form of Equation 6 which intercept at Ω_{crit}. If no prior assumption of Ω_{crit} is made, a single function combining the two linear regimes with a flexible intercept is needed.

To this end, we used the error function

$$\operatorname{erf}(x) = \frac{2}{\sqrt{\pi}} \int_0^x e^{-t^2}\, dt \tag{7}$$

multiplied by two linear functions of the form $f(x) = ax + b$ to get

$$\begin{aligned} y = \; & (0.5 \cdot (+\operatorname{erf}(p \cdot (x + x_{intcp})) + 1) \cdot (a_2 x + b_2)) \\ & + (0.5 \cdot (-\operatorname{erf}(p \cdot (x + x_{intcp})) + 1) \cdot (a_1 x + b_1))) \end{aligned} \tag{8}$$

where $y \equiv (\log_{10} r)$, $b \equiv (\log_{10} k)$, $a \equiv n$, and $x \equiv \log_{10}(1 - \Omega)$ from Equation 6. $x_{intcp} = \frac{b_1 - b_2}{a_2 - a_1}$ is the intercept of the two linear functions, which is Ω_{crit}, and p is a term that determines how rounded the corner is where the two linear functions meet (here: $p = 80$). f_1 represents the slower dissolution regime for $\Omega_{\text{crit}} < \Omega < 1$ and f_2 the faster one for $\Omega < \Omega_{\text{crit}}$.

The fitting of the data points is achieved with SciPy's curve_fit function (SciPy version 1.7.3 (Virtanen et al., 2020)) using initial guesses of $n_1 = 0$, $n_2 = 3$, $\log_{10} k_1 = -3.5$, and $\log_{10} k_2 = -1.5$.

3. Results and Discussion

3.1. Description of Compiled In Situ Measurements

The compiled data set consists of 752 data points. The experiments used diverse sets of samples, such as deep-sea sediments made up of foraminiferal assemblages, synthetic calcite crystals, coccolithophores, pteropods, or high-Mg calcite ooids. Nonetheless, only a fifth of the samples consist of aragonite and less than half are of biogenic origin. All measurements were made in the northern hemisphere, with the majority (551 measurements; 73%) in

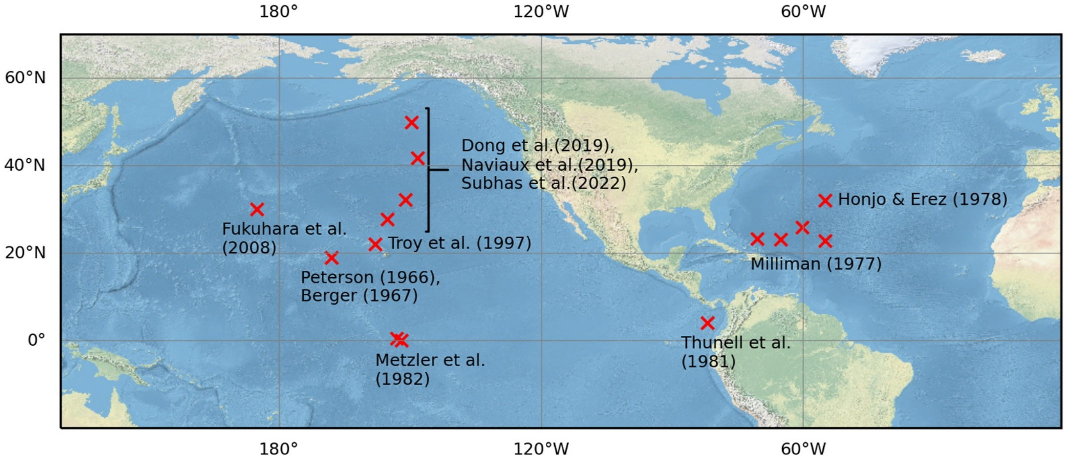

Figure 3. Locations of in situ dissolution rate measurements.

the Pacific (Figure 3), where the water is more corrosive and dissolution is expected at shallower depths. The remainder of the measurements (studies M77 and HE78) were made in the Sargasso Sea in the subtropical North Atlantic. Even though the experiments do not cover all ocean basins, the experiment sites still capture a wide range of marine environments (Figure S12 in Supporting Information S1).

The most frequent way to measure dissolution was determining the weight loss of a carbonate mineral sample that was placed on a mooring (surface or subsurface mooring) and exposed to seawater for a specific amount of time. A small portion of studies place their samples in devices that cycled the seawater around the sample to avoid diffusion effects (15% of samples). Apart from weight loss, two other methods have been used to determine dissolution. One, based on $\delta^{13}C$, was developed by Subhas et al. (2015) and is used by the studies that were part of the CDisK-IV cruise (67 measurements; 9%). The other used surface roughness as a proxy for dissolution (T97; 14 measurements; 1.8%). A couple of studies additionally record fragmentation of their samples as an indicator of dissolution (T81 and M82; 79 measurements; 11%). The dissolution rate is reported either mass-normalized (percentage weight loss per day; 668 measurements; 89%) or mass- and surface area-normalized (hereafter referred to as surface-normalized; g cm^{-2} d^{-1}; 163 measurements; 22%), or for HE78 and the CDisK-IV studies, both are provided (80 measurements; 11%).

There is a wide range in the number of measurements each study made: T81 and T97 contain only 14 measurements each, while F08 contains 298 measurements, making up 40% of the data set (Table 1). A large number of measurements does not necessarily mean a wide range of saturation states: for aragonite in the F08 data set, Ω is always below 0.6 (Figure 4b). All F08 data are from deeper than 1,000 m (Figure 5), so shallower $CaCO_3$

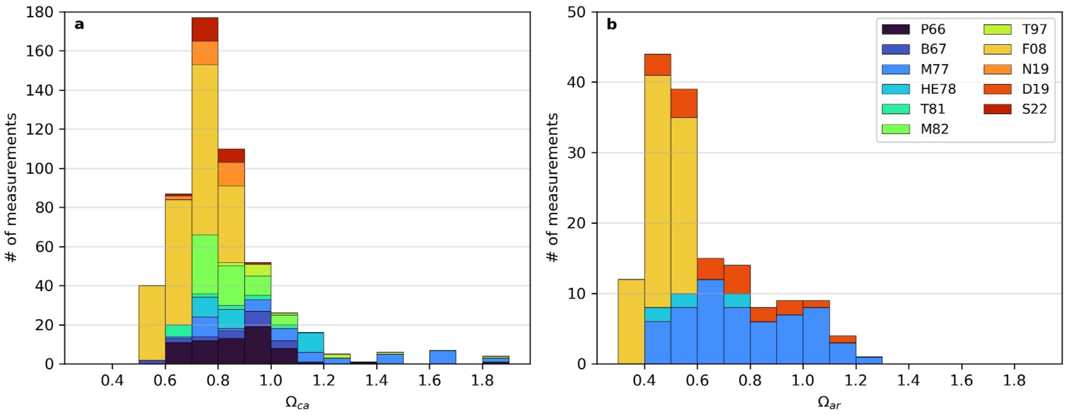

Figure 4. Number of measurements for Ω bins (step-size: 0.1), for (a) calcite and (b) aragonite (note the different scale on y-axis). Measurements with Ω > 2 are omitted (7 measurements). The different studies are color-coded.

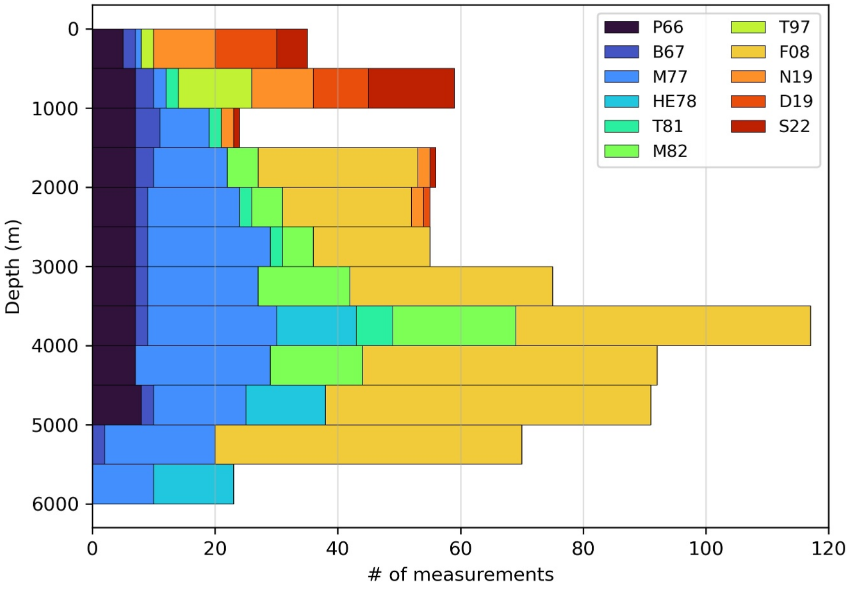

Figure 5. Depth-distribution of the compiled data set (bin width: 500 m).

dissolution cannot be investigated with their data. Conversely, the CDisK-IV studies mostly measured dissolution in the upper 1,000 m. The greatest ranges of depth and saturation states for both calcite and aragonite were achieved by the M77 experiments (162 measurements; 22%).

There is a clear trend of higher dissolution rate at lower Ω (Figure 6). Near the saturation horizon ($\Omega = 1$), greater variability in the data and uncertainty in Ω make the trends more unclear. Since dissolution under these conditions is slower, the rates are closer to the limit of detection and therefore the signal-to-noise ratio is higher. In general, the uncertainty in Ω decreases with depth (Figure S13 in Supporting Information S1) because at depth there is less variability in temperature, salinity and oxygen through time.

Dissolution rates at the same saturation state are spread across 2 orders of magnitude even at dissolution further from the saturation horizon. Since almost no studies report uncertainties for their dissolution rate measurements (except P66 who gave a constant measurement uncertainty of $\pm 3.3 \times 10^{-5}$ g cm^{-2} d^{-1} and the CDisK-IV data with their unique δ^{13}C method), it is difficult to say how much of the variation in the rates can be attributed to measurement uncertainty. However, even studies that used two of the same kinds of samples at one depth for controls did not see such a spread in measurements as in Figure 6. Whether this can be attributed to the differences in experimental design is examined in Section 3.2.

Mass-normalized (Figure 6a) and surface-normalized dissolution rates (Figure 6b) cannot be directly compared with each other if no measurements of the surface area were reported. The different units can serve different purposes: surface-normalized in situ data is better suited for comparisons to laboratory measurements since those results are often expressed this way, while mass-normalized data works better for model comparisons because models usually only track the mass of particulate inorganic carbon (PIC) in the water column and not its surface area.

Because surface-normalized data try to account for differences in sample size, it is tempting to assume that they are superior to mass-normalized data (In general, smaller samples have a greater surface-to-mass ratio than larger samples, so if samples of different sizes were mass-normalized then we would expect the smaller samples to dissolve faster). However, it is questionable which (if any) method of measuring surface area can capture the reactive surface area that is actually available for dissolution (Cubillas et al., 2005). For example, Brunauer-Emmett-Teller (BET) analysis determine the specific surface area (SSA) through gas-adsorption, but it has been argued that preparation of biogenic samples forms micropores which are captured by BET measurements but are unreactive and unavailable for dissolution (Jeschke & Dreybrodt, 2002; Walter & Morse, 1985). Additionally, complex surface shapes can lead to decreased dissolution due to mass-transport limitations (Fukuhara et al., 2008; Sulpis et al., 2022). Because the reactive surface area is not captured, surface area measurements can be an

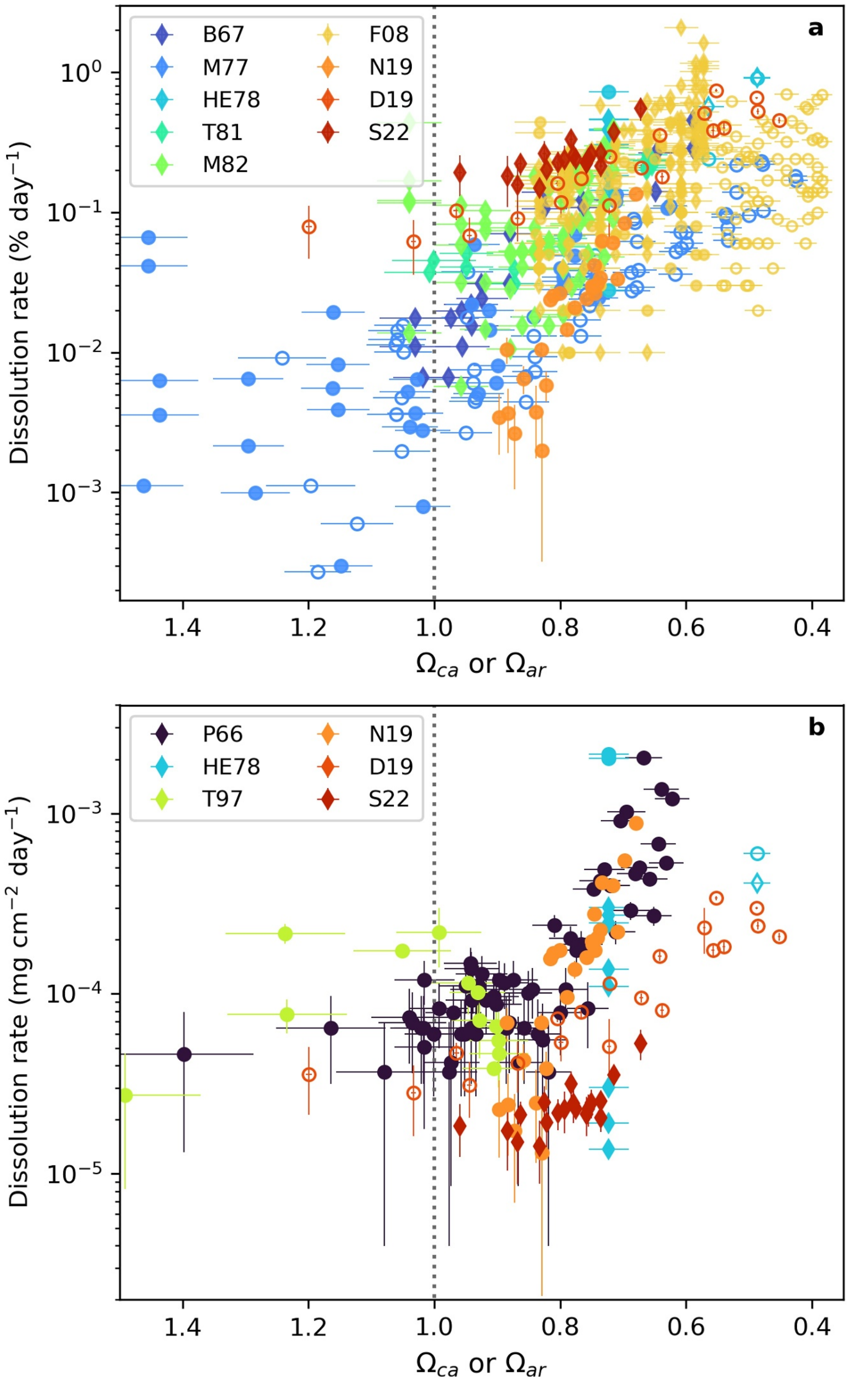

Figure 6. (a) Mass-normalized and (b) surface-normalized dissolution rate as a function of Ω. Open markers denote aragonite, closed markers calcite. Biogenic samples are marked with a diamond and inorganic samples with a circle. Error bars show the 1σ uncertainty in Ω and, if available, the measured dissolution rate (the latter only available for P66, D19, N19, and S22). Data points with $\Omega > 1.5$ are not shown.

additional source of uncertainty. This is demonstrated by HE78: the dissolution of 13 different sample types was measured and the rates were expressed as both mass-normalized and surface-normalized. For all samples containing calcite at 5,518 m depth, the spread of measured dissolution rates was just over one order of magnitude when normalized to mass but over two orders of magnitude when normalized to mass and surface area.

Additionally, if the surface area was not determined with the same method then the data will not be comparable between studies. In the studies presented here, P66 approximates the surface area geometrically, assuming the calcite spheres used were smooth, ignoring potential pits and fractures, Milliman (1977) later notes that the surface area might have been underestimated by a factor of 5 (Milliman (1977) is a correction to nowadays more widely cited Milliman (1975), with the earlier paper expressing dissolution in surface-normalized terms that the same author later recognizes as erroneous). More recent studies suggest that the difference in crystal surface area (roughness) might result in variability in dissolution rates of up to two orders of magnitude (Agrawal et al., 2021; Lüttge et al., 2013; Wolthers et al., 2012). The P66 rates in Figure 6 can therefore be regarded as an upper bound for the dissolution rate. On the other hand, HE78, N19, D19, and S22 determine the specific surface area (SSA) by BET measurements (HE78 with helium gas and N19, D19, and S22 with krypton gas) which results in higher surface areas than the geometric approximations and therefore it is expected that on average they obtain lower dissolution rates in their experiments, representing a lower bound for the dissolution rate.

Another issue with surface areas becomes apparent in T97: the surface area changes throughout the dissolution process, depending on which dissolution mechanism is prevalent. In that study, the dissolution rate was determined by measuring surface area roughness with Atomic Force Microscopy (AFM). They first assumed a smooth surface and then equated any increase in roughness with dissolution taking place. However, close to equilibrium ($\Omega = 1$), dissolution happens through step edge retreat which can instead smoothen the surface as edges retreat to the edge of a crystal and disappear. Dissolution is therefore limited by the number of existing steps on the reactive surface. This mechanism also offers a possible explanation for why the dissolution rate in T97 unexpectedly decreases with Ω: if more dissolution actually decreases the number of edges instead of forming new etch pits, then surface roughness will not be able to capture the amount of dissolution that actually took place.

The change of surface area with ongoing dissolution introduces another problem, especially for studies that last several months. HE78 measured the SSA before and after their experiment and found that the surface area changes were sample-dependent: while for the foraminiferal assemblage the SSA doubled or even tripled, for the coccoliths it increased by only 10%. The surface-normalized dissolution rate therefore also changes throughout experiments to varying degrees, complicating comparisons between studies or even between samples within a study. Further investigations into how surface area and therefore rate of dissolution change throughout the dissolution process are warranted.

To circumvent these issues with surface-normalized dissolution rates, we use only the mass-normalized rates in the following analysis and discussion.

3.2. What Drives Dissolution and How Big Is the Effect of Differing Experimental Design?

To investigate the reason for the large spread in the rate measurements for a given saturation state, a machine learning model was trained to predict the mass-normalized dissolution rate from Ω and various features of the experimental design (Section 2.4).

The model achieved an R^2 of 0.824 on the test set, so the majority of the variance in dissolution rate was explained. The RMSE and MAE are 0.079% day^{-1} and 0.049% day^{-1}. The model predicts faster dissolution rates reasonably well but the lower the dissolution rate, the higher the relative error becomes, especially for dissolution rates below 0.01% day^{-1} (Figure 7). This is due to using squared error as the learning objective for the model, meaning, small absolute errors (which would be large relative errors for low dissolution rates) are “punished” less when the model is trained, leading to worse predictions for the very low rates. However, those rates have higher inherent uncertainty due to being close to the level of detection, so we prioritized good model performance for the higher rates. The worse performance for low dissolution rates could also point to underfitting, meaning that the model was too simple or lacked the flexibility to capture the underlying patterns in the data, resulting in higher prediction errors. But due to the small number of measurements, increasing the model complexity would likely lead to overfitting, where the model captures noise and random variability in the data at the expense of the meaningful underlying patterns. We therefore consider the model used to be the best trade-off between complexity and accuracy.

In Figure 8, the model has been used to predict dissolution rates for a range of different saturation states with all possible combinations of the different experimental design choices that have been made in the in situ studies. The

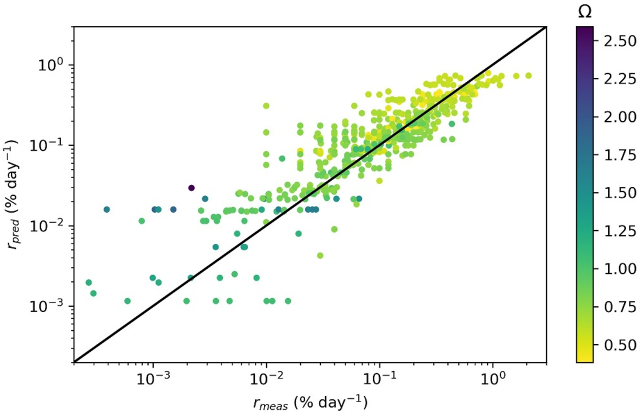

Figure 7. Model predictions of the dissolution rate plotted against the actual measurements.

spread in predicted dissolution rates for each Ω matches the spread in the actual data. This demonstrates that the different experimental design decisions (e.g., sample size and type, mesh size,…) used in the various studies can explain the range of variation in measured dissolution rates at any given Ω.

Permutation feature importance gives insight into the relevance of each feature for the model prediction by measuring the increase in the model's prediction error (here, MSE) when permuting one feature. Features with permuted (random) values cannot meaningfully contribute to the prediction because the relationship between the feature and the true outcome has been broken. In a PFI analysis, this enables us to assess how much worse the model performs if one feature is not present. Our PFI analysis shows that by far the most important feature is Ω. All other features in the model have a contribution that is at most almost an order of magnitude smaller. For the measurement method of dissolution and the material of the sample (calcite/aragonite, assuming the same Ω), the contributions are completely insignificant (Figure S14 in Supporting Information S1).

A drawback of PFI is that the importance of correlated features is shared between them and some features of the experimental design do co-vary. For instance, the deployment time was always very short when dissolution was measured via the δ^{13}C method. The importance of the measurement method might therefore be underestimated and that of the deployment time overestimated, or vice versa, by our PFI analysis. However, since the design of the experiment and the water chemistry are mostly independent, our conclusion that the measured dissolution rates are mainly determined by Ω should still hold.

Partial dependence plots visualize the influence of every predictor in the model on the predicted dissolution rate by showing the average predicted rate for a feature if every data point in the data set is forced to a certain value of this feature while all other features are kept the same. This reveals the form of the relationship the feature has with the predicted outcome, which could be linear, logarithmic, logistic, or more complex. If we have some mechanistic understanding of the real-world system (i.e., we know at least qualitatively what the relationships between predictors and the model output should be), then PDPs can help to check whether the model makes sense.

Figure 9 shows the PDPs for all features that were used to train the model. For most of the features, the relationships shown are intuitive and expected: for stronger undersaturation (lower Ω), the model predicts higher dissolution rates (Figure 9a). The jaggedness of the line probably results from the datapoints not being evenly distributed along the Ω range or could be a sign of overfitting, where the PDP is trying to fit the noise in the data. The bigger the size of the sample, the lower the mass-normalized dissolution rate, since

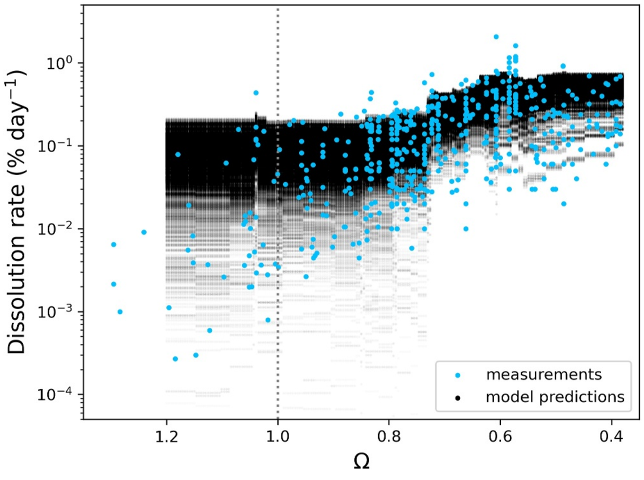

Figure 8. Model predictions for a range of saturation states with all possible combinations of experimental design choices (e.g., sample size and type, mesh size,…, see Section 2.4).

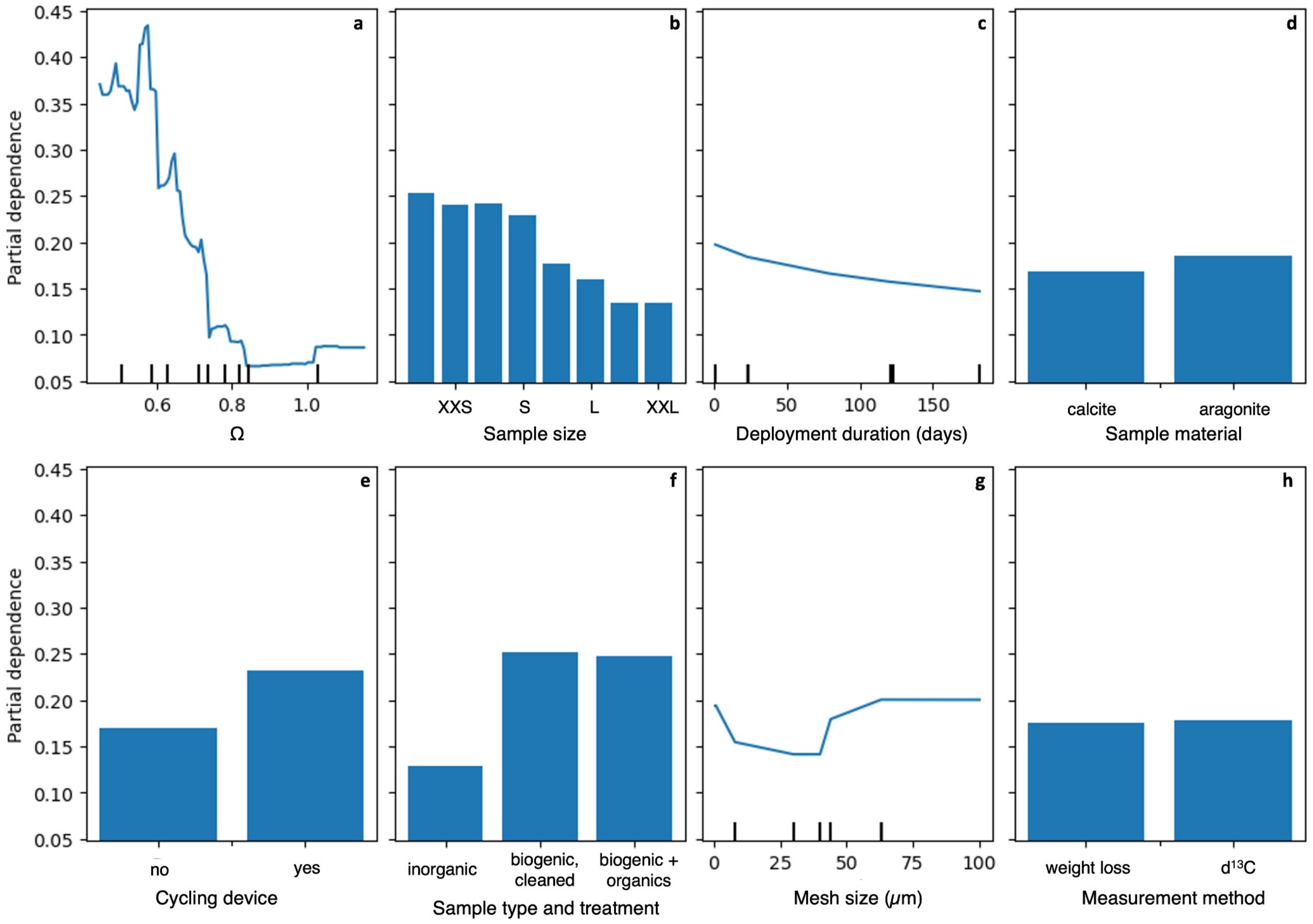

Figure 9. Partial dependence of the predicted dissolution rate for all features used in the regression model. Continuous features are represented as a line graph and categorical features as bar graphs. The black lines on the x-axis for continuous features indicate the deciles (10% quantiles). The y-axis is the average predicted dissolution rate.

less surface area is available for dissolution (Figure 9b). Biogenic samples are predicted to have on average higher dissolution rates than inorganic samples (Figure 9f), which matches our understanding that biogenic samples have a higher defect density and therefore should dissolve faster (e.g., as seen by Busenberg and Niel Plummer (1989)). However, whether the biogenic samples underwent an oxidative cleaning protocol (bleaching) to remove organic coatings does not affect the model outcome significantly. This is only directly compared in B67 and HE78 where bleaching the samples increased the dissolution rate. The presence of a cycling device also leads to higher predictions of dissolution rates (Figure 9e). This could be due to dissolution not being transport-limited (Batchelor-McAuley et al., 2022; Fan et al., 2022) or because the water flow could break off small pieces of $CaCO_3$ which leads to increased weight loss and therefore erroneous rate observations (as in Metzler et al. (1982)).

For mesh size, the relationship is more complex. We expected that coarser meshes would lead to higher dissolution rates for two reasons: (a) finer mesh might restrict water flow around the sample, leading to a pool of water with elevated Ω being trapped around the sample, thus inhibiting dissolution (while some studies, e.g., the CDisK-IV studies, have tested this and made sure that dissolution is not transport limited, this is not the case for all), and (b) coarser mesh might lead to mechanical loss of the sample which would result in falsely high dissolution rates (as described in Metzler et al. (1982)). However, the model predicts the lowest dissolution rates at intermediate mesh sizes (Figure 9g). One possible reason for this is the lack of training data for mesh sizes above 80 μm. Another issue is the assumption of independence of the features in PDPs (Molnar, 2022). When PDPs are calculated, new data points are generated by averaging over marginal distributions of other features. These new data points might be unlikely (i.e., very small meshes have only been chosen in combination with water cycling devices when stationary water is not a problem) or completely unrealistic (i.e., a mesh size that is larger than the size of the sample), which in turn distorts the apparent dependence of the prediction on this feature.

There are several ways in which deployment duration can affect the dissolution rate. If the dissolution mechanism leads to increased surface area (as seen in HE78, where SSA was measured both before and after deployment) through etch pit formation, then mass-normalized dissolution should reflect that with increased rates for experiments with longer durations. The opposite seems to be the case here (Figure 9c). One reason could be that the prevalent dissolution mechanism actually decreases the surface area as mentioned in the previous section. Additionally, sample preparation often involved crushing the samples which might have created a greater reactive surface area at the beginning of the deployment. Dissolution is then expected to slow down once the initial freshly exposed layer has been dissolved.

The gradient (or "flatness") of the PDP curves can also indicate feature importance (Greenwell et al., 2018), assuming that the more the partial dependence values of a feature vary, the more important that feature is. The results in Figure 9 show similar patterns as the PFI results in Figure S14 in Supporting Information S1: the partial dependence of predicted dissolution rate changes rapidly with respect to Ω (Figure 9a), indicating its relatively high importance as a predictor, whereas for the material of the sample (Figure 9d) and the measurement method (Figure 9h) there is almost no difference in the partial dependence for the different possible predictions, suggesting lower importance.

In summary, this machine learning approach is a useful tool that helps us analyze quantitatively how different features can influence a measured variable by training a model to predict said variable based on those features. Even though complex tree-based models often cannot be interpreted directly, several methods exist to help us make sense of them. Here, the model was able to capture much of the underlying patterns of the data, which for the most part matched our real-world qualitative understanding of how design choices should affect the dissolution rate and additionally showed which features affect it at the most. In practice, this means that only studies designed similarly can be compared directly, with the most important design choices for inter-compatibility being the particle sizes, inorganic versus biogenic samples, and the presence or absence of a device that cycles the water around the samples.

3.3. What Can In Situ Measurements Tell Us Despite Differences in the Experimental Design?

While our analysis indicated that the majority of the variance in the dissolution rate was driven by Ω, the differences in experimental design were still significant. Therefore, while absolute rates might be less meaningful, the patterns of variation with depth, Ω, and other environmental variables can still give useful insights.

As examples, we explore two phenomena in more detail: (a) dissolution above the saturation horizon and (b) existence and variability of a critical saturation state Ω_{crit}.

3.3.1. Dissolution Above the Saturation Horizon

While laboratory experiments measure dissolution only when the bulk water is undersaturated, alkalinity measurements in the ocean indicate that a substantial amount of carbonate mineral dissolution happens close to the surface where the seawater is oversaturated. With our new Ω estimates we can now examine whether in situ studies have also measured dissolution in such conditions.

Most studies do not include a significant number of measurements far above the saturation horizon. Most experiments have been conducted in the Pacific, where Ω values are on average lower than in other ocean basins and experiments have generally been focused on depths where water was known or assumed to be close to equilibrium or undersaturated. One exception is T97. They measure the highest dissolution rate of their iceland spar calcite samples at and above the saturation horizon at 550 and 600 m (in two separate experiments, 4 months apart). The authors interpret this as being caused by respiration of organic matter in the surrounding seawater, forming acids that attack the calcite surface (Troy et al., 1997). It has been shown that carbonic anhydrase enhances dissolution by etching the surface of the calcite sample, with the greatest effect close to equilibrium (Dong et al., 2020; Subhas et al., 2017). This might have played a role as well. We do not focus on this example further due to the issues with the measurement method that we described in Section 3.1.

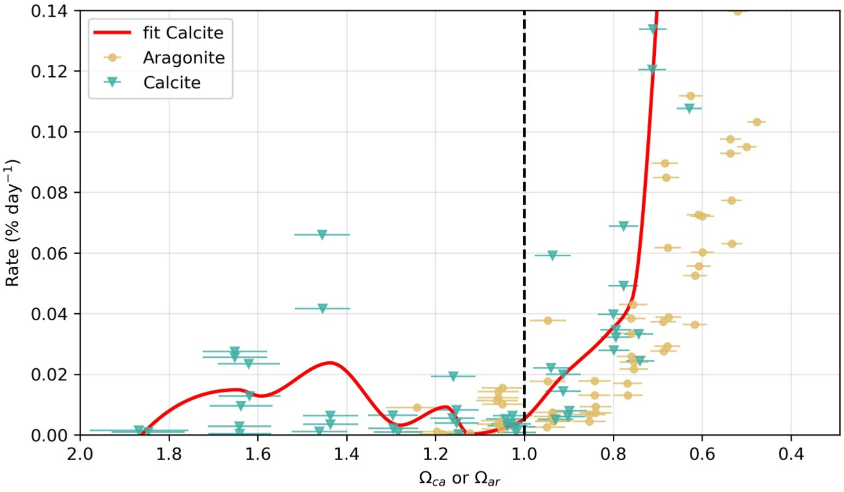

Figure 10. Dissolution rate measurements at the four stations of the M77 experiments for the calcite and aragonite samples as a function of Ω. The error bars represent the uncertainty in Ω. The fit was produced by binning the calcite dissolution rates in Ω-bins of 0.05 and interpolating over the bin-averaged rates.

Another exception is M77 (Figure 4). Below the saturation horizon, dissolution follows the expected pattern of increasing non-linearly with lower saturation states (Figure 10). However, at 3 out of 4 stations where dissolution experiments were conducted, M77 also observed significant dissolution of their calcite samples at $1.7 > \Omega_{ca} > 1.4$. This local maximum occurs at 2,000–2,500 m depth (Figure S16 in Supporting Information S1), which is far above the local saturation horizon for calcite, at approximately 4,300 m. This pattern of dissolution with depth does not match the patterns that are found when estimating dissolution from alkalinity budgets (Feely et al., 2002; Sulpis et al., 2021)—there, dissolution is highest closest to the surface, reaching a minimum at around 1,000 m, before gradually increasing again. So, what else could cause this local dissolution maximum?

Usually, three possible explanations are given for dissolution in apparently oversaturated waters: (a) the presence of a more soluble form of carbonate mineral, such as Mg calcite (Feely et al., 2002; Wilson et al., 2009; Woosley et al., 2012), (b) dissolution in the more acidic environment of zooplankton guts (Jansen & Wolf-Gladrow, 2001; Milliman et al., 1999; Pond et al., 1995), and (c) other micro-environments, such as marine snow aggregates, where bacterial oxidation of organic matter can enhance the dissolution process (Alldredge & Cohen, 1987; Jansen & Wolf-Gladrow, 2001; Subhas et al., 2022).

Hypothesis (i) does not apply in this case because we know that the calcite samples consisted of planktonic foraminifera, primarily *Orbulina universa* and *Trilobatus sacculifer* which contain little magnesium (<2%) (Nürnberg et al., 1996). Hypothesis (ii) is equally unlikely: zooplankton live mainly in the epipelagic and mesopelagic layer (<1,000 m) (Fernández de Puelles et al., 2019), and the samples were in bags of fine mesh (<40 μm), so they could not have been consumed by other organisms.

Organic coatings were left intact in M77 and several hundred foraminifera made up one sample, which could be similar to the marine snow aggregate in hypothesis (iii). Additionally, bacteria and more organic matter could have become stuck on the mesh or the sample when it passed through surface waters during deployment. This leaves open the possibility that organic matter degradation could have led to a more acidic micro-environment. To evaluate the influence of (iii), we calculated Ω_{metab} which was proposed by Subhas et al. (2022) to account for the degradation and consumption of organic matter in aggregates where organic carbon and $CaCO_3$ are closely packed together. Ω_{metab} is calculated from revised ambient DIC and TA values, which are determined assuming that all dissolved oxygen in the bulk seawater is metabolized (upper limit for aerobic metabolic activity). Although Ω_{metab} was proposed for marine snow particles and not for carbonate samples artificially placed in mesh bags, it can provide the lower limit for the saturation state inside the sample. While the metabolic saturation

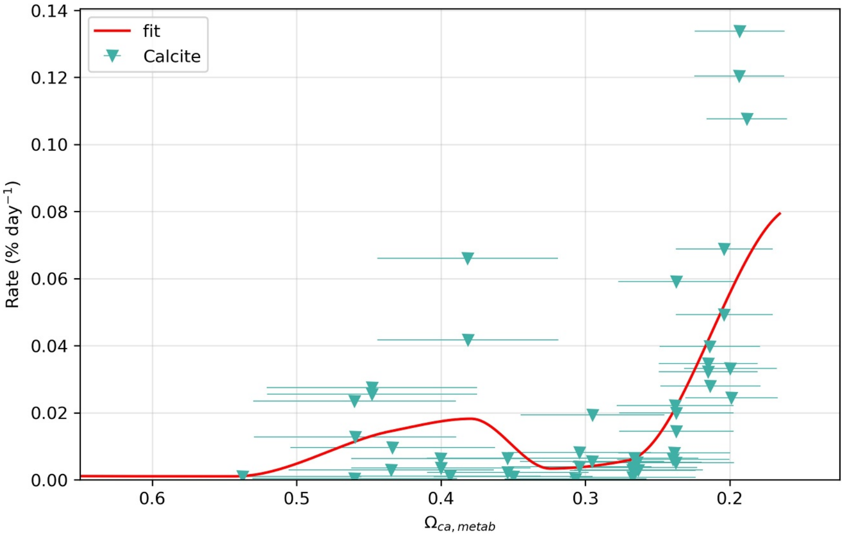

Figure 11. Dissolution rate measurements at the four stations of the M77 experiments for the calcite samples as a function of Ω_{metab}, which was calculated following Subhas et al. (2022). The error bars show the same uncertainty as the original Ω values. The fit was produced by binning the calcite dissolution rates in Ω_{metab}-bins of 0.05 and interpolating over the bin-averaged rates.

horizon of calcite is indeed shallower than the minimum sample depth, so the dissolution no longer appears to have occurred in undersaturated waters, the pattern with Ω_{metab} does not follow Equation 6 (i.e., monotonically increasing) but still has a local maximum (Figure 11) that requires a different explanation. To explain this peak, more is needed. One possibility is the presence of a catalyst that increased the rate of dissolution, such as carbonic anhydrase, as observed by Subhas et al. (2017). Another possibility is that the continued respiration and dissolution proceeded together in a ratio such that the waters stay undersaturated. However, these hypotheses cannot be further examined due to the lack of relevant data. Ultimately, an undersaturated micro-environment due to metabolic activity could explain why dissolution is possible at this depth, but on its own it is insufficient to explain the localized peak at 2,000–2,500 m.

There are more possibilities beyond the three usual explanations discussed above. For instance, (iv) dissolved organic carbon (DOC) binding calcium (Ca) through a chelate effect and thereby lowering the saturation state. Ca has a high affinity to form complexes with organic matter (Raspor et al., 1980), leading to a lower amount of Ca_{free} than what has been calculated from salinity. However, while the DOC concentration is ∼50 μmol kg^{-1} (Hansell et al., 2021), the Ca concentration is several orders of magnitude larger at ∼10 mmol kg^{-1}. The effect of Ca dilution would therefore be negligible. Another hypothesis is that (v) the $Ca:CO_3$ ratio can affect dissolution, which could also be influenced by complexation of Ca. Stack and Grantham (2010) observed features of dissolution on calcite crystals in oversaturated water at a $Ca:CO_3$ ratio of 22:1 (highest ratio tested). At the locations and depths of the M77 stations, $Ca:CO_3$ ratio increases with depth from 110:1 to 190:1. If high $Ca:CO_3$ ratios allowed dissolution in oversaturated water, then this effect would be true for all samples in the experiment, not just at certain depths, making (v) highly unlikely.

Finding the main driver of this local peak in dissolution would allow us to understand whether it was a consequence of the experiment design, whether it is geographically constrained, and whether it also applies to sinking or suspended particles in the water column. If no explanation is found that describes how dissolution was thermodynamically possible, then (vi) measurement errors would need to be invoked. However, since the duplicates at each depth and at stations separated both temporally (by several months) and spatially (by hundreds of kilometers) showed the same pattern, this seems unlikely. Additionally, the aragonite and high-Mg calcite ooids (for which no saturation state could be estimated), show the same dissolution pattern with depth as the calcite samples at some stations, which suggests that the effect is decoupled from the exact particle type. Ultimately, we are unable to explain the dissolution pattern with Ω in M77 with the data available. It is not the only study with a

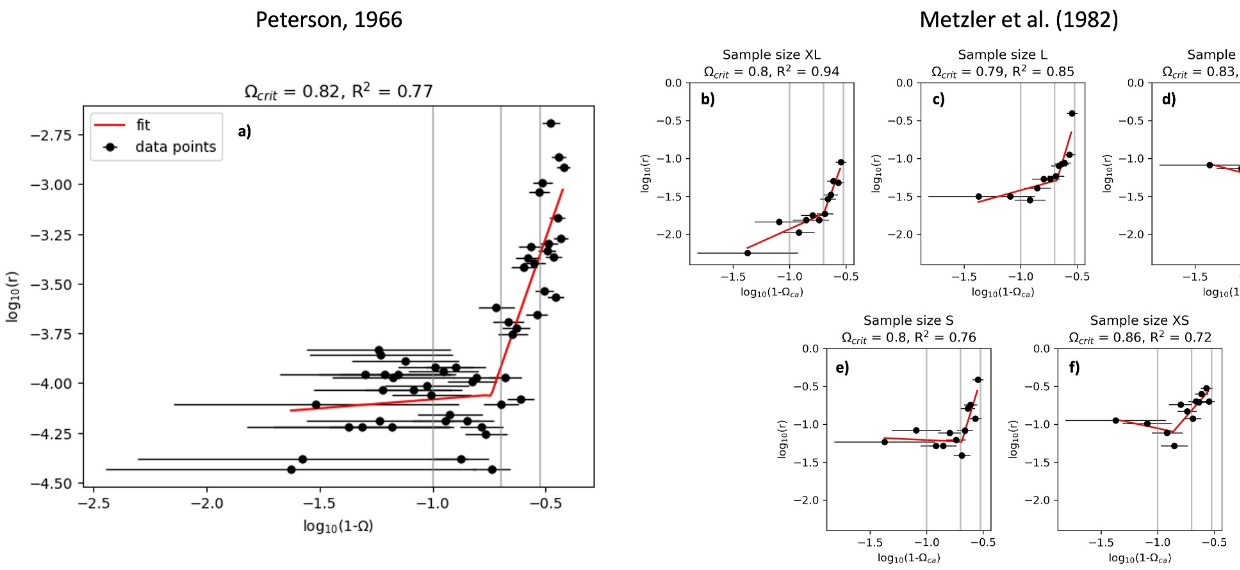

Figure 12. Ω_{crit} for dissolution rates (a) for the calcite pieces in P66 and (b)–(f) foraminifera in different size fractions in M82, determined by fitting to Equation 8. The gray vertical lines mark the saturation state at $\Omega = 0.9$, 0.8 and 0.7 from left to right. The Ω_{crit} value producing the best fit and its corresponding R^2 value are given above each panel.

peak in the dissolution rate above the saturation horizon (see T97) and if similar features are seen in future studies as well, measurement of a broader set of auxiliary variables could provide a resolution.

3.3.2. Dissolution Regimes

Many in situ studies observe that dissolution starts to rapidly increase at a certain depth (seen most clearly in P66) at a critical amount of undersaturation. The surface-normalized data in our compilation also show a faster increase in dissolution rate with declining Ω at saturation states lower than $\Omega = 0.8$ (Figure 6b). The same is not immediately obvious for the mass-normalized data (Figure 6a) due to the greater scatter in measured rates. However, the PDP for Ω (based on the model trained on mass-normalized data only) supports the existence of a change in dissolution rate at a certain Ω value. When Ω is close to equilibrium, the dissolution rate is barely affected by Ω, but for $\Omega \lesssim 0.75$ the curve becomes much steeper, demonstrating a stronger influence of Ω on the measured dissolution rate (Figure 9a).

Based on the laboratory measurements of Naviaux, Subhas, Rollins, et al. (2019), N19 and S22 divided their rate measurements into two dissolution regimes, with the boundary at $\Omega_{\mathrm{crit}} = 0.80$ and $\Omega_{\mathrm{crit}} = 0.78$ respectively. However, it is unclear whether these Ω_{crit} values also produce the best fit for dissolution in the water column. Other properties (e.g., pressure and dissolution inhibitors) can affect Ω_{crit} and have been investigated in the laboratory (Dong et al., 2018; Naviaux, Subhas, Dong, et al., 2019) but not with field data, which will always include some extra forms of variability and complexity that can never be fully reproduced in a laboratory setting. Here, we fit the dissolution rates in the compilation to two dissolution regimes with a flexible Ω_{crit} (Section 2.5). This works best for studies that have a high Ω resolution over the relevant Ω range from 0.65 to 0.95.

For P66 and M82, the best fit was achieved with Ω_{crit} between 0.80 and 0.87, with $R^2 > 0.7$ (Figure 12). For comparison, assuming only one dissolution regime with no Ω_{crit} gave $R^2 < 0.5$ for the same data, a less good fit. The reaction order for the dissolution regime where $\Omega < \Omega_{\mathrm{crit}}$, n_2, was 3.2 for P66 and for M82 it varied between 1.7 (Sample size XS) and 5.0 (Sample size L). This large difference in n_2 for the size fractions in M82 is mainly explained by the different values of Ω_{crit}: the further from equilibrium Ω_{crit}, the larger n_2. Contrary to our expectations, dissolution slightly decreases with decreasing saturation for the three smallest size fractions. Several other studies showed similar patterns (Figure S17 in Supporting Information S1; M77, T81, F08). This may be due to the uncertainty in the Ω estimation or to measurement errors (not reported in those studies) but we do not

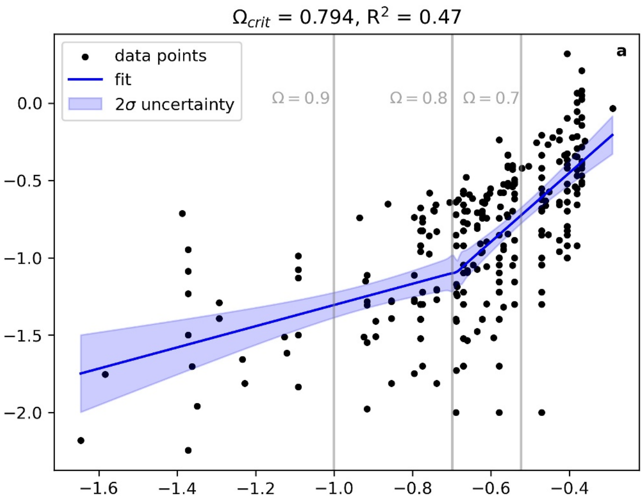

Figure 13. Dissolution rate as a function of Ω_{crit} for all mass-normalized biogenic samples in the compilation. The gray vertical lines mark the saturation state at $\Omega = 0.9$, 0.8 and 0.7 from left to right. The Ω_{crit} value producing the best fit and its corresponding R^2 value are given above the graph.

have the necessary information to investigate this further. Examining more studies, it shows that for this kind of analysis a wide range of Ω with a high resolution of measurements is needed for the most plausible results. The results vary widely if the study has either few samples or covers a small Ω range: the best fitting Ω_{crit} value is sometimes as low as 0.6 or as high as 0.95, whereas sometimes none is found at all and n_2 varies from 0.9 to 15 (Figure S17 in Supporting Information S1).

Combining all studies with biogenic $CaCO_3$ samples (the difference in solubility for calcite and aragonite is already accounted for in the mineral-specific Ω value and assuming that the dissolution rate is the same for each mineral at the same Ω (supported by Figure 9d)), the best fit for mass-normalized dissolution rates was achieved at $\Omega_{\text{crit}} = 0.8$ (Figure 13) with

$$r_{\text{slow}} = 10^{-0.62(\pm 0.15)} \cdot (1 - \Omega)^{0.68(\pm 0.16)} \tag{9}$$

$$r_{\text{fast}} = 10^{0.44(\pm 0.13)} \cdot (1 - \Omega)^{2.2(\pm 0.2)} \tag{10}$$

$n_2 = 2.2(\pm 0.2)$ is inside the uncertainty of S22 ($n_2 = 2.1(\pm 0.5)$) but higher than D19 ($n_2 = 1.76(\pm 0.36)$) which used inorganic samples. It is significantly lower than N19 ($n_2 = 4.7(\pm 0.7)$).

The effects of the different experimental designs lead to a large spread in the data, resulting in a worse fit than in Figure 12, where individual studies were examined separately. Since the dissolution rate is greatly affected by the origin of the sample (biogenic or inorganic, Figure 9f), only biogenic samples were included here. To further reduce the spread of the results, they should be further divided, for instance by size fraction or whether water cycling devices were employed. However, in the current data set this would reduce the number of samples such that no good fits would be possible because too small an Ω range would be covered.

The Ω_{crit} chosen when fitting measurements to Equation 6 significantly affects n_2 (reaction order of the fast dissolution regime): with $\Omega_{\text{crit}} = 0.75$, $n_2 = 2.8$ but with $\Omega_{\text{crit}} = 0.85$, n_2 is just 1.9. For calcite, the effect is minimal in the ocean, since Ω rarely reaches below 0.6 and at $\Omega = 0.6$, the dissolution rate with $\Omega_{\text{crit}} = 0.75$ is only 10% faster than with $\Omega_{\text{crit}} = 0.85$. Furthermore, the dissolution rate for calcite at $\Omega = 0.6$ is only increased by 35% when using two dissolution regimes with an intermediate $\Omega_{\text{crit}} = 0.80$ instead of only one with no Ω_{crit} (Figure 14). However, for aragonite, Ω can be around 0.4 at depth. Pteropod shells can sink several hundred meters per day (Noji et al., 1997), hence they can reach depths with such low saturation states, possibly with further implications such as reducing calcite dissolution by dissolving deeper than expected thus raising Ω (Sulpis et al., 2022). At $\Omega = 0.4$, the shifting of Ω_{crit} closer or further away from equilibrium when fitting the data also has more substantial effects: the dissolution rate with $\Omega_{\text{crit}} = 0.75$ is 25% faster than with $\Omega_{\text{crit}} = 0.80$ and 55% faster than with $\Omega_{\text{crit}} = 0.85$. Most notably, the dissolution rate for aragonite at $\Omega = 0.4$ more than doubles (+106%) when using two dissolution regimes with an intermediate $\Omega_{\text{crit}} = 0.80$ instead of only one with no Ω_{crit} (Figure 14).

Overall, the in situ studies suggest that Ω_{crit} is slightly closer to equilibrium in the water column than the results of the lab experiments by Naviaux, Subhas, Rollins, et al. (2019) ($\Omega_{\text{crit}} = 0.80$ instead of $\Omega_{\text{crit}} = 0.75$). As a consequence, our compilation of in situ data suggest that dissolution rates at depth may be slightly lower for calcite (up to ∼3%) and significantly lower for aragonite (up to ∼20%) in the real ocean than would be expected from laboratory experiments.

4. Conclusion

In situ experiments account for more real-world complexities than laboratory experiments can. However, published data have not been fully utilized because of missing hydrographic variables which would make experiments conducted at different study locations and/or decades apart comparable. Our approach of combining WOA data together with CANYON-B to estimate a set of carbonate system and other ancillary variables helps to overcome this issue, adding value to the published data by allowing us to more directly compare them with each

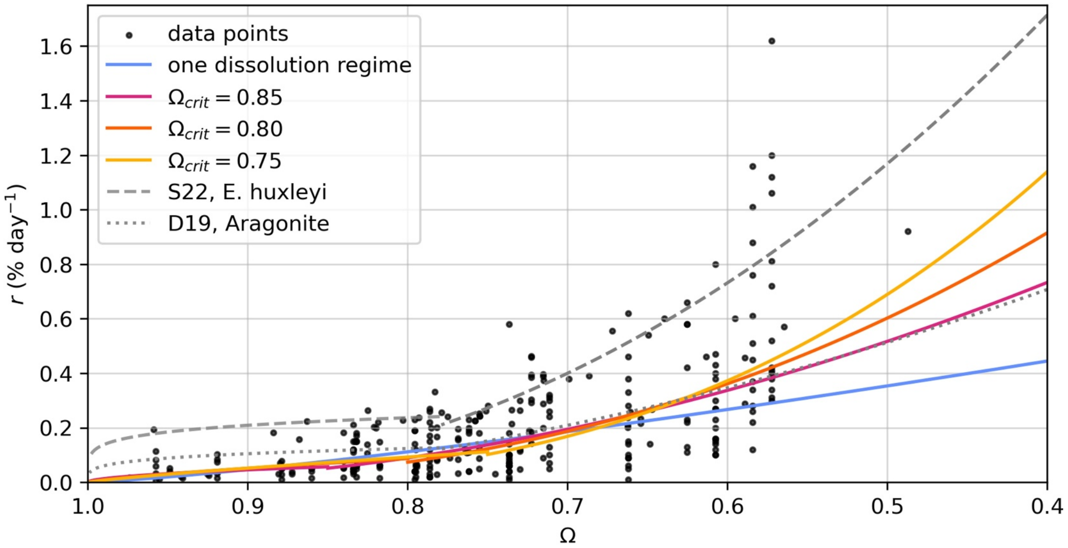

Figure 14. Dissolution rate as a function of Ω, where the rate measurements of biogenic samples were fitted to different Ω_{crit} values or no Ω_{crit} (no change in dissolution mechanism) at all. The fits for the D19 and S22 data (Subhas et al., 2022, Table 2) are plotted in gray for comparison.

other. Our approach could also be applied to other types of experiments and published data sets that do not include a complete set of ancillary hydrographic variables.

In the case of carbonate mineral dissolution we were able to show a wide spread of dissolution rates at the same Ω. While this is partly explained by the choice of sample material, other decisions regarding the experimental design, such as a water cycling device (that removes diffusive transport limitations) and the duration of the deployment, also play a non-negligible role. As a result, the absolute values of measured dissolution rates still cannot be directly compared, but the more qualitative patterns of dissolution rate and its relationship with Ω in the water column still can be.

Future experiments should focus on samples representing the exported inorganic carbon. Past studies use carbonate minerals that are inorganic or were collected from sediments, which might have less realistic shapes and have long lost any organic coatings that might have initially be present. We suggest studies to use samples that resemble actual sinking carbonate particles as closely as possible, such as well-preserved planktonic foraminifera or pteropods. Aragonite has been underrepresented in the studies so far, only making up 20% of samples and mainly being investigated by only three studies, M77, F08, and D19, which for the most part used inorganic aragonite. A water cycling device might eliminate any transport limitation completely, which is ideal for assessing the true surface kinetics. However, this might be unrealistic for slow sinking particles and could also lead to particles breaking up more easily into smaller pieces, therefore enhancing dissolution artificially. Additionally, such mixing devices are more resource intensive (e.g., batteries, pumps) and might therefore come at the expense of fewer/shallower experiment depths and a smaller range of Ω that is investigated. A possible solution is to measure the effect on the dissolution rate when using a mixing device in the lab and the in situ measurements of dissolution rates in simple mesh bags can then be adjusted accordingly. Reporting both mass-normalized and surface-normalized rates allows the comparison to more studies, both laboratory and modeling.

Our analysis confirms that dissolution starts to increase more rapidly at $\Omega_{crit} \approx 0.8$, confirming that the results of laboratory experiments are applicable in the ocean. To better constrain Ω_{crit}, future in situ studies should consider measuring dissolution rates with a higher resolution over a wider range of saturation states, as well as performing crystallographic investigations (e.g., AFM) to assess which mechanisms contributed primarily to dissolution at different Ω values.

We also found that the only experiment that was conducted in significantly oversaturated water did observe dissolution above the saturation horizon, although no satisfactory explanation for this could be found. Due to the lack of ancillary variables, the large scatter in the existing data and the uncertainty of the estimated variables, it was not possible to investigate inhibitors to dissolution or other drivers of dissolution, apart from Ω. Conducting more in situ experiments in a range of different marine environments (e.g., Pacific and Atlantic) but with the same experimental design and sample types and with the extensive measurement of ancillary variables, such as carbonate system parameters, could help to disentangle the effects of other variables and close the major gaps in our fundamental understanding of marine carbonate mineral dissolution.

Data Availability Statement

The compiled data set with all the added ancillary information can be found in Cala and Humphreys (2023). The Python and MATLAB scripts to compile the data and estimate Ω as well as the Python script to generate all the figures in the main text and the Supporting Information S1 is available in Cala (2023).

Acknowledgments

The authors would like thank all the scientists and crews who over the last six decades collected and published the in situ dissolution rates on which this analysis is based on. This research was funded by the UU-NIOZ collaboration project, “BEYΩND the known drivers of marine carbonate mineral dissolution: closing the gap in the alkalinity budget” (project number NZ4543.25). This project has received funding from the European Research Council (ERC) under the European Union's Horizon 2020 research and innovation programme (grant agreement No. [819588]). OS was supported by the Netherlands Organization for Scientific Research (NWO-VENI Grant VI.Veni.212.086).

References

Agrawal, P., Bollermann, T., Raoof, A., Iliev, O., Fischer, C., & Wolthers, M. (2021). The contribution of hydrodynamic processes to calcite dissolution rates and rate spectra. *Geochimica et Cosmochimica Acta*, *307*, 338–350. https://doi.org/10.1016/j.gca.2021.05.003

Alldredge, A. L., & Cohen, Y. (1987). Can microscale chemical patches persist in the sea? Microelectrode study of marine snow, fecal pellets. *Science*, *235*(4789), 689–691. https://doi.org/10.1126/science.235.4789.689

Archer, D., Eby, M., Brovkin, V., Ridgwell, A., Cao, L., Mikolajewicz, U., et al. (2009). Atmospheric lifetime of fossil fuel carbon dioxide. *Annual Review of Earth and Planetary Sciences*, *37*(1), 117–134. https://doi.org/10.1146/annurev.earth.031208.100206

Batchelor-McAuley, C., Yang, M., Rickaby, R. E. M., & Compton, R. G. (2022). Calcium carbonate dissolution from the laboratory to the ocean: Kinetics and mechanism. *Chemistry—A European Journal*, *28*(68), e202202290. https://doi.org/10.1002/chem.202202290

Berelson, W. M., Adkins, J. F., Subhas, A. V., Dong, S., & Naviaux, J. D. (2022). In situ experimentally determined dissolution rates of biogenic calcites along a North Pacific transect between Hawaii and Alaska (KM1712 expedition) in August 2017. *Biological and Chemical Oceanography Data Management Office (BCO-DMO)*. https://doi.org/10.26008/1912/BCO-DMO.856409.2

Berger, W. H. (1967). Foraminiferal Ooze: Solution at depths. *Science*, *156*(3773), 383–385. https://doi.org/10.1126/science.156.3773.383

Bittig, H. C., Steinhoff, T., Claustre, H., Fiedler, B., Williams, N. L., Sauzède, R., et al. (2018). An alternative to static climatologies: Robust estimation of open ocean CO_2 variables and nutrient concentrations from T, S, and O_2 data using Bayesian neural networks. *Frontiers in Marine Science*, *5*. https://doi.org/10.3389/fmars.2018.00328

Breiman, L. (2001a). Random forests. *Machine Learning*, *45*(1), 5–32. https://doi.org/10.1023/A:1010933404324

Breiman, L. (2001b). Statistical modeling: The two cultures (with comments and a rejoinder by the author). *Statistical Science*, *16*(3), 199–231. https://doi.org/10.1214/ss/1009213726

Breiman, L., Friedman, J., Stone, C. J., & Olshen, R. A. (1984). *Classification and regression trees*. CRC Press.

Busenberg, E., & Niel Plummer, L. (1989). Thermodynamics of magnesian calcite solid-solutions at 25°C and 1 atm total pressure. *Geochimica et Cosmochimica Acta*, *53*(6), 1189–1208. https://doi.org/10.1016/0016-7037(89)90056-2

Cala, B. A. (2023). In-situ-dissolution-compilation [Software]. *GitHub*. Retrieved from https://github.com/bcala1/in-situ-dissolution-compilation

Cala, B. A., & Humphreys, M. P. (2023). Synthesis of in situ marine calcium carbonate dissolution kinetic measurements in the water column—Data [Data]. *NIOZ*. https://doi.org/10.25850/nioz/7b.b.bg

Chen, T., & Guestrin, C. (2016). XGBoost: A scalable tree boosting system. In *Proceedings of the 22nd ACM SIGKDD international conference on knowledge discovery and data mining* (pp. 785–794). Association for Computing Machinery. https://doi.org/10.1145/2939672.2939785

Cubillas, P., Köhler, S., Prieto, M., Chaïrat, C., & Oelkers, E. H. (2005). Experimental determination of the dissolution rates of calcite, aragonite, and bivalves. *Chemical Geology*, *216*(1), 59–77. https://doi.org/10.1016/j.chemgeo.2004.11.009

Dickson, A. G. (1990). Standard potential of the reaction: AgCl(s) + 12H2(g) = Ag(s) + HCl(aq), and and the standard acidity constant of the ion HSO4- in synthetic sea water from 273.15 to 318.15 k. *The Journal of Chemical Thermodynamics*, *22*(2), 113–127. https://doi.org/10.1016/0021-9614(90)90074-Z

Dong, S., Berelson, W. M., Adkins, J. F., Rollins, N. E., Naviaux, J. D., Pirbadian, S., et al. (2020). An atomic force microscopy study of calcite dissolution in seawater. *Geochimica et Cosmochimica Acta*, *283*, 40–53. https://doi.org/10.1016/j.gca.2020.05.031

Dong, S., Berelson, W. M., Rollins, N. E., Subhas, A. V., Naviaux, J. D., Celestian, A. J., et al. (2019). Aragonite dissolution kinetics and calcite/aragonite ratios in sinking and suspended particles in the North Pacific. *Earth and Planetary Science Letters*, *515*, 1–12. https://doi.org/10.1016/j.epsl.2019.03.016

Dong, S., Subhas, A. V., Rollins, N. E., Naviaux, J. D., Adkins, J. F., & Berelson, W. M. (2018). A kinetic pressure effect on calcite dissolution in seawater. *Geochimica et Cosmochimica Acta*, *238*, 411–423. https://doi.org/10.1016/j.gca.2018.07.015

Edmond, J. M. (1974). On the dissolution of carbonate and silicate in the deep ocean. *Deep-Sea Research and Oceanographic Abstracts*, *21*(6), 455–480. https://doi.org/10.1016/0011-7471(74)90094-1

Fan, X., Batchelor-McAuley, C., Yang, M., & Compton, R. G. (2022). Single calcite particle dissolution kinetics: Revealing the influence of mass transport. *ACS Measurement Science Au*, *2*(5), 422–429. https://doi.org/10.1021/acsmeasuresciau.2c00025

Feely, R. A., Sabine, C. L., Lee, K., Millero, F. J., Lamb, M. F., Greeley, D., et al. (2002). In situ calcium carbonate dissolution in the Pacific Ocean. *Global Biogeochemical Cycles*, *16*(4), 91–1–91–12. https://doi.org/10.1029/2002GB001866

Fernández de Puelles, M. L., Gazá, M., Cabanellas-Reboredo, M., Santandreu, M. D. M., Irigoien, X., González-Gordillo, J. I., et al. (2019). Zooplankton abundance and diversity in the tropical and subtropical ocean. *Diversity*, *11*(11), 203. https://doi.org/10.3390/d11110203

Friedman, J. H. (2001). Greedy function approximation: A gradient boosting machine. *Annals of Statistics*, *29*(5), 1189–1232. https://doi.org/10.1214/aos/1013203451

Fukuhara, T., Tanaka, Y., Ioka, N., & Nishimura, A. (2008). An in situ experiment of calcium carbonate dissolution in the central Pacific Ocean. *International Journal of Greenhouse Gas Control*, *2*(1), 78–88. https://doi.org/10.1016/S1750-5836(07)00085-0

Garcia, H., Weathers, K., Paver, C., Smolyar, I., Boyer, T., Locarnini, M., et al. (2019). World Ocean Atlas 2018, volume 3: Dissolved oxygen, apparent oxygen utilization, and dissolved oxygen saturation. Retrieved 2023-05-16, from https://archimer.ifremer.fr/doc/00651/76337/

Gehlen, M., Bassinot, F. C., Chou, L., & McCorkle, D. (2005). Reassessing the dissolution of marine carbonates: II. Reaction kinetics. *Deep Sea Research Part I: Oceanographic Research Papers*, *52*(8), 1461–1476. https://doi.org/10.1016/j.dsr.2005.03.011

Greenwell, B. M., Boehmke, B. C., & McCarthy, A. J. (2018). A simple and effective model-based variable importance measure. https://doi.org/10.48550/arXiv.1805.04755

Hansell, D. A., Carlson, C. A., Amon, R. M. W., Álvarez Salgado, X. A., Yamashita, Y., Romera-Castillo, C., & Bif, M. B. (2021). *Compilation of dissolved organic matter (DOM) data obtained from global ocean observations from 1994 to 2021. Version 2. (NCEI Accession 0227166)*. NOAA National Centers for Environmental Information. https://doi.org/10.25921/S4F4-YE35

Hawley, J., & Pytkowicz, R. M. (1969). Solubility of calcium carbonate in seawater at high pressures and 2°C. *Geochimica et Cosmochimica Acta*, *33*(12), 1557–1561. https://doi.org/10.1016/0016-7037(69)90156-2

Honjo, S., & Erez, J. (1978). Dissolution rates of calcium carbonate in the deep ocean; an in-situ experiment in the North Atlantic Ocean. *Earth and Planetary Science Letters*, *40*(2), 287–300. https://doi.org/10.1016/0012-821X(78)90099-7

Humphreys, M. P., Lewis, E. R., Sharp, J. D., & Pierrot, D. (2022). PyCO2SYS v1.8: Marine carbonate system calculations in Python. *Geoscientific Model Development*, *15*(1), 15–43. https://doi.org/10.5194/gmd-15-15-2022

Jansen, H., & Wolf-Gladrow, D. (2001). Carbonate dissolution in copepod guts: A numerical model. *Marine Ecology Progress Series*, *221*, 199–207. https://doi.org/10.3354/meps221199

Jeschke, A. A., & Dreybrodt, W. (2002). Dissolution rates of minerals and their relation to surface morphology. *Geochimica et Cosmochimica Acta*, *66*(17), 3055–3062. https://doi.org/10.1016/S0016-7037(02)00893-1

Keir, R. S. (1980). The dissolution kinetics of biogenic calcium carbonates in seawater. *Geochimica et Cosmochimica Acta*, *44*(2), 241–252. https://doi.org/10.1016/0016-7037(80)90135-0

Knecht, N. S., Benedetti, F., Hofmann Elizondo, U., Bednaršek, N., Chaabane, S., de Weerd, C., et al. (2023). The impact of zooplankton calcifiers on the marine carbon cycle. *Global Biogeochemical Cycles*, *37*(6), e2022GB007685. https://doi.org/10.1029/2022GB007685

Liang, H., Lunstrum, A. M., Dong, S., Berelson, W. M., & John, S. G. (2023). Constraining $CaCO_3$ export and dissolution with an ocean alkalinity inverse model. *Global Biogeochemical Cycles*, *37*(2), e2022GB007535. https://doi.org/10.1029/2022GB007535

Locarnini, M., Mishonov, A., Baranova, O., Boyer, T., Zweng, M., Garcia, H., et al. (2018). World Ocean Atlas 2018, volume 1: Temperature. Retrieved from https://archimer.ifremer.fr/doc/00651/76338/

Lüttge, A., Arvidson, R. S., & Fischer, C. (2013). A stochastic treatment of crystal dissolution kinetics. *Elements*, *9*(3), 183–188. https://doi.org/10.2113/gselements.9.3.183

Metzler, C. V., Wenkam, C. R., & Berger, W. H. (1982). Dissolution of foraminifera in the eastern equatorial Pacific; an in situ experiment. *Journal of Foraminiferal Research*, *12*(4), 362–368. https://doi.org/10.2113/gsjfr.12.4.362

Milliman, J. D. (1975). Dissolution of aragonite, Mg-calcite, and calcite in the North Atlantic Ocean. *Geology*, *3*(8), 461–462. https://doi.org/10.1130/0091-7613(1975)3⟨461:DOAMAC⟩2.0.CO;2

Milliman, J. D. (1977). Dissolution of calcium carbonate in the Sargasso Sea (northwest Atlantic). In *The fate of fossil fuel CO_2 in the Oceans* (pp. 641–653). https://doi.org/10.1007/978-1-4899-5016-1_32

Milliman, J. D., Troy, P. J., Balch, W. M., Adams, A. K., Li, Y. H., & Mackenzie, F. T. (1999). Biologically mediated dissolution of calcium carbonate above the chemical lysocline? *Deep Sea Research Part I: Oceanographic Research Papers*, *46*(10), 1653–1669. https://doi.org/10.1016/S0967-0637(99)00034-5

Molnar, C. (2022). Interpretable machine learning: A guide for making black box models explainable (2nd ed.). Retrieved from https://christophm.github.io/interpretable-ml-book/

Morse, J. W., & Arvidson, R. S. (2002). The dissolution kinetics of major sedimentary carbonate minerals. *Earth-Science Reviews*, *58*(1), 51–84. https://doi.org/10.1016/S0012-8252(01)00083-6

Morse, J. W., & Berner, R. A. (1972). Dissolution kinetics of calcium carbonate in sea water; I, A kinetic origin for the lysocline. *American Journal of Science*, *272*(9), 840–851. https://doi.org/10.2475/ajs.272.9.840

Mucci, A. (1983). The solubility of calcite and aragonite in seawater at various salinities, temperatures, and one atmosphere total pressure. *American Journal of Science*, *283*(7), 780–799. https://doi.org/10.2475/ajs.283.7.780

Naviaux, J. D., Subhas, A. V., Dong, S., Rollins, N. E., Liu, X., Byrne, R. H., et al. (2019). Calcite dissolution rates in seawater: Lab vs. in-situ measurements and inhibition by organic matter. *Marine Chemistry*, *215*, 103684. https://doi.org/10.1016/j.marchem.2019.103684

Naviaux, J. D., Subhas, A. V., Rollins, N. E., Dong, S., Berelson, W. M., & Adkins, J. F. (2019). Temperature dependence of calcite dissolution kinetics in seawater. *Geochimica et Cosmochimica Acta*, *246*, 363–384. https://doi.org/10.1016/j.gca.2018.11.037

Neukermans, G., Bach, L. T., Butterley, A., Sun, Q., Claustre, H., & Fournier, G. R. (2023). Quantitative and mechanistic understanding of the open ocean carbonate pump—Perspectives for remote sensing and autonomous in situ observation. *Earth-Science Reviews*, *239*, 104359. https://doi.org/10.1016/j.earscirev.2023.104359

Noji, T. T., Bathmann, U. V., Bodungen, B. V., Voss, M., Antia, A., Krumbholz, M., et al. (1997). Clearance of picoplankton-sized partides and formation of rapidly sinking aggregates by the pteropod, *Limacina reiroversa*. *Journal of Plankton Research*, *19*(7), 863–875. https://doi.org/10.1093/plankt/19.7.863

Nürnberg, D., Bijma, J., & Hemleben, C. (1996). Assessing the reliability of magnesium in foraminiferal calcite as a proxy for water mass temperatures. *Geochimica et Cosmochimica Acta*, *60*(5), 803–814. https://doi.org/10.1016/0016-7037(95)00446-7

Olsen, A., Key, R. M., van Heuven, S., Lauvset, S. K., Velo, A., Lin, X., et al. (2016). The global ocean data analysis project version 2 (GLODAPv2)—An internally consistent data product for the world ocean. *Earth System Science Data*, *8*(2), 297–323. https://doi.org/10.5194/essd-8-297-2016

Orr, J. C., Epitalon, J.-M., Dickson, A. G., & Gattuso, J.-P. (2018). Routine uncertainty propagation for the marine carbon dioxide system. *Marine Chemistry*, *207*, 84–107. https://doi.org/10.1016/j.marchem.2018.10.006

Pedregosa, F., Varoquaux, G., Gramfort, A., Michel, V., Thirion, B., Grisel, O., et al. (2011). Scikit-learn: Machine learning in Python. *Journal of Machine Learning Research*, *12*(85), 2825–2830. Retrieved from http://jmlr.org/papers/v12/pedregosa11a.html

Peterson, M. N. A. (1966). Calcite: Rates of dissolution in a vertical profile in the central Pacific. *Science*, *154*(3756), 1542–1544. https://doi.org/10.1126/science.154.3756.1542

Pond, D. W., Harris, R. P., & Brownlee, C. (1995). A microinjection technique using a pH-sensitive dye to determine the gut pH of *Calanus helgolandicus*. *Marine Biology*, *123*(1), 75–79. https://doi.org/10.1007/BF00350325

Raspor, B., Nürnberg, H. W., Valenta, P., & Branica, M. (1980). Kinetics and mechanism of trace metal chelation in sea water. *Journal of Electroanalytical Chemistry and Interfacial Electrochemistry*, *115*(2), 293–308. https://doi.org/10.1016/S0022-0728(80)80333-0

Rohatgi, A. (2021). Webplotdigitizer: Version 4.5. Retrieved from https://automeris.io/WebPlotDigitizer

Stack, A. G., & Grantham, M. C. (2010). Growth rate of calcite steps as a function of aqueous calcium-to-carbonate ratio: Independent attachment and detachment of calcium and carbonate ions. *Crystal Growth & Design*, *10*(3), 1409–1413. https://doi.org/10.1021/cg901395z

Subhas, A. V., Adkins, J. F., Rollins, N. E., Naviaux, J., Erez, J., & Berelson, W. M. (2017). Catalysis and chemical mechanisms of calcite dissolution in seawater. *Proceedings of the National Academy of Sciences of the United States of America*, *114*(31), 8175–8180. https://doi.org/10.1073/pnas.1703604114

Subhas, A. V., Dong, S., Naviaux, J. D., Rollins, N. E., Ziveri, P., Gray, W., et al. (2022). Shallow calcium carbonate cycling in the North Pacific Ocean. *Global Biogeochemical Cycles*, *36*(5), e2022GB007388. https://doi.org/10.1029/2022GB007388

Subhas, A. V., Rollins, N. E., Berelson, W. M., Dong, S., Erez, J., & Adkins, J. F. (2015). A novel determination of calcite dissolution kinetics in seawater. *Geochimica et Cosmochimica Acta*, *170*, 51–68. https://doi.org/10.1016/j.gca.2015.08.011

Sulpis, O., Agrawal, P., Wolthers, M., Munhoven, G., Walker, M., & Middelburg, J. J. (2022). Aragonite dissolution protects calcite at the seafloor. *Nature Communications*, *13*(1), 1104. https://doi.org/10.1038/s41467-022-28711-z

Sulpis, O., Jeansson, E., Dinauer, A., Lauvset, S. K., & Middelburg, J. J. (2021). Calcium carbonate dissolution patterns in the ocean. *Nature Geoscience*, *14*(6), 423–428. https://doi.org/10.1038/s41561-021-00743-y

Sulpis, O., Lauvset, S. K., & Hagens, M. (2020). Current estimates of K_1* and K_2* appear inconsistent with measured CO_2 system parameters in cold oceanic regions (preprint). *Data Assimilation/Chemical Tracers/Surface/All Geographic Regions*. https://doi.org/10.5194/os-2020-19

Teng, H. H. (2004). Controls by saturation state on etch pit formation during calcite dissolution. *Geochimica et Cosmochimica Acta*, *68*(2), 253–262. https://doi.org/10.1016/S0016-7037(03)00423-X

Thunell, R. C., Keir, R. S., & Honjo, S. (1981). Calcite dissolution: An in situ study in the Panama Basin. *Science*, *212*(4495), 659–661. https://doi.org/10.1126/science.212.4495.659

Troy, P. J., Li, Y.-H., & Mackenzie, F. T. (1997). Changes in surface morphology of calcite exposed to the oceanic water column. *Aquatic Geochemistry*, *3*(1), 1–20. https://doi.org/10.1023/A:1009652821575

Uppström, L. R. (1974). The boron/chlorinity ratio of deep-sea water from the Pacific Ocean. *Deep-Sea Research and Oceanographic Abstracts*, *21*(2), 161–162. https://doi.org/10.1016/0011-7471(74)90074-6

Virtanen, P., Gommers, R., Oliphant, T. E., Haberland, M., Reddy, T., Cournapeau, D., et al. (2020). SciPy 1.0: Fundamental algorithms for scientific computing in Python. *Nature Methods*, *17*(3), 261–272. https://doi.org/10.1038/s41592-019-0686-2

Walter, L. M., & Morse, J. W. (1985). The dissolution kinetics of shallow marine carbonates in seawater: A laboratory study. *Geochimica et Cosmochimica Acta*, *49*(7), 1503–1513. https://doi.org/10.1016/0016-7037(85)90255-8

Wilson, R. W., Millero, F. J., Taylor, J. R., Walsh, P. J., Christensen, V., Jennings, S., & Grosell, M. (2009). Contribution of fish to the marine inorganic carbon cycle. *Science*, *323*(5912), 359–362. https://doi.org/10.1126/science.1157972

Wolthers, M., Nehrke, G., Gustafsson, J. P., & Van Cappellen, P. (2012). Calcite growth kinetics: Modeling the effect of solution stoichiometry. *Geochimica et Cosmochimica Acta*, *77*, 121–134. https://doi.org/10.1016/j.gca.2011.11.003

Woosley, R. J., Millero, F. J., & Grosell, M. (2012). The solubility of fish-produced high magnesium calcite in seawater. *Journal of Geophysical Research*, *117*(C4), C04018. https://doi.org/10.1029/2011JC007599

Zeebe, R. E., & Wolf-Gladrow, D. (2001). *CO_2 in seawater: Equilibrium, kinetics, isotopes*. Gulf Professional Publishing. (Google-Books-ID: g3j3Zn4kEscC).

Zweng, M., Reagan, J., Seidov, D., Boyer, T., Locarnini, M., Garcia, H., et al. (2019). World Ocean Atlas 2018. *Salinity*, *2*. Retrieved from https://archimer.ifremer.fr/doc/00651/76339/

References From the Supporting Information

Dong, S., Liu, X., Naviaux, J. D., Subhas, A. V., Rollins, N. E., Adkins, J. F., & Berelson, W. M. (2022). Carbonate chemistry and CTD data collected along a North Pacific transect between Hawaii and Alaska on R/V Kilo Moana cruise KM1712 in August 2017. *Biological and Chemical Oceanography Data Management Office (BCO-DMO)*. https://doi.org/10.26008/1912/BCO-DMO.836954.2

Lauvset, S. K., Lange, N., Tanhua, T., Bittig, H. C., Olsen, A., Kozyr, A., et al. (2022). GLODAPv2.2022: The latest version of the global interior ocean biogeochemical data product. *Earth System Science Data*, *14*(12), 5543–5572. https://doi.org/10.5194/essd-14-5543-2022

Patsavas, M. C., Byrne, R. H., Wanninkhof, R., Feely, R. A., & Cai, W.-J. (2015). Internal consistency of marine carbonate system measurements and assessments of aragonite saturation state: Insights from two U.S. coastal cruises. *Marine Chemistry*, *176*, 9–20. https://doi.org/10.1016/j.marchem.2015.06.022